Exploring Potential Mechanisms for the Initiation of Solifluction Patterns

Rachel C. Glade[1,2*], JohnPaul Sleiman[1], Alice Quillen[3], David Cúñez[1], Sarah Williams[1]

[1]Department of Earth and Environmental Sciences, University of Rochester, Rochester 14580, USA.

[2]Department of Mechanical Engineering, University of Rochester, Rochester 14580, USA.

[3]Department of Physics, University of Rochester, Rochester 14580, USA.

*Corresponding author. Email: rachel.glade@rochester.edu

Exploring Potential Mechanisms for the Initiation of Solifluction Patterns

Rachel C. Glade[1,2*], JohnPaul Sleiman[1], Alice Quillen[3], David Cúñez[1], Sarah Williams[1]

[1]Department of Earth and Environmental Sciences, University of Rochester, Rochester 14580, USA.

[2]Department of Mechanical Engineering, University of Rochester, Rochester 14580, USA.

[3]Department of Physics, University of Rochester, Rochester 14580, USA.

*Corresponding author. Email: rachel.glade@rochester.edu

Hillslopes in arctic regions commonly display large-scale features—known as solifluction patterns—that form due to the exceedingly slow downhill movement of frost-heaved soil. Here we use a combination of remote sensing data, linear stability analysis, numerical modeling, and review of a wide range of literature to evaluate several working hypotheses for the necessary and sufficient conditions needed to form solifluction patterns. We find that despite striking visual similarity, fluid buckling, wrinkling, dripping, and roll wave patterns are not directly analogous to solifluction patterns. However, broadly inspired by non-inertial instabilities observed in shear-thickening oobleck, we propose a conceptual framework for the formation of solifluction instabilities that relies on spatial heterogeneity of soil velocities in the presence of random topographic bumps. More broadly, this study illustrates both caveats and the potential for success in drawing inspiration from diverse fields to understand pattern formation in the complex granular/fluid materials on Earth's surface.

1 Introduction

Periglacial hillslopes subjected to frequent freeze-thaw cycles commonly host distinctive spatial soil patterns including sorted circles and stripes (*1*), frost wedge polygons (*2*), and solifluction terraces and lobes (*3, 4*), which we focus on in this paper (Fig1 A,B). Originally coined by (*5*) to mean the downslope motion of saturated soil in any environment, the term "solifluction" is now generally used to describe downslope periglacial soil motions that occur due to a combination of two processes: 1) frost creep, in which soil is lofted normal to the slope in the winter as ice lenses form within the soil (*6, 7*), then settles vertically in the spring as the soil thaws, resulting in a net downslope motion (*6, 8*) and 2) gelifluction, in which partially-to-fully saturated soil flows downslope for a brief period of time during spring thaw (*9, 10*). Together these processes lead to slow downslope displacements on order of mms to cms per year (*11*). A ubiquitous erosional process in cold regions on Earth and potentially on Mars (*12–14*), solifluction is especially relevant as the need to predict and mitigate slope stability due to thawing permafrost becomes increasingly urgent (*15*). However, while much work has been done to characterize these features in the field (*3, 3, 11, 16, 17*) and in the lab (*18–20*), our understanding of the physical underpinnings of solifluction and the resulting patterns remains limited. This stems from the complexity of the rheology of icy soils—which exhibit seasonally variable strong heterogeneity in grain size, water and ice content (*4*) and can behave both as a fluid and solid under different conditions (*21*)—as well as the difficulty in obtaining accurate and sufficient measurements for very slow-moving soils that exist in logistically challenging field locations.

Solifluction patterns may be broken into two distinct parts: terraces, which are wavelike patterns oriented downslope, and lobes, which are finger-like patterns that form cross-slope, often (but not always) at terrace fronts. A recent study argued that cross-slope solifluction lobe formation may be analogous to finger-like instabilities found at the front of surface-tension dominated fluid flows known as "contact line instabilities," such as paint dripping down a wall or oil fingering in a frying pan (*4*). In this framework, (*4*) proposed that competition between gravity and enhanced soil cohesion (or another mechanism of stalling) results in the formation of lobes, analogous to competition between the driving force and surface tension in thin film flows (*24*). The authors show that a scaling analysis based on fluid-like motions of soil can capture the first order characteristics

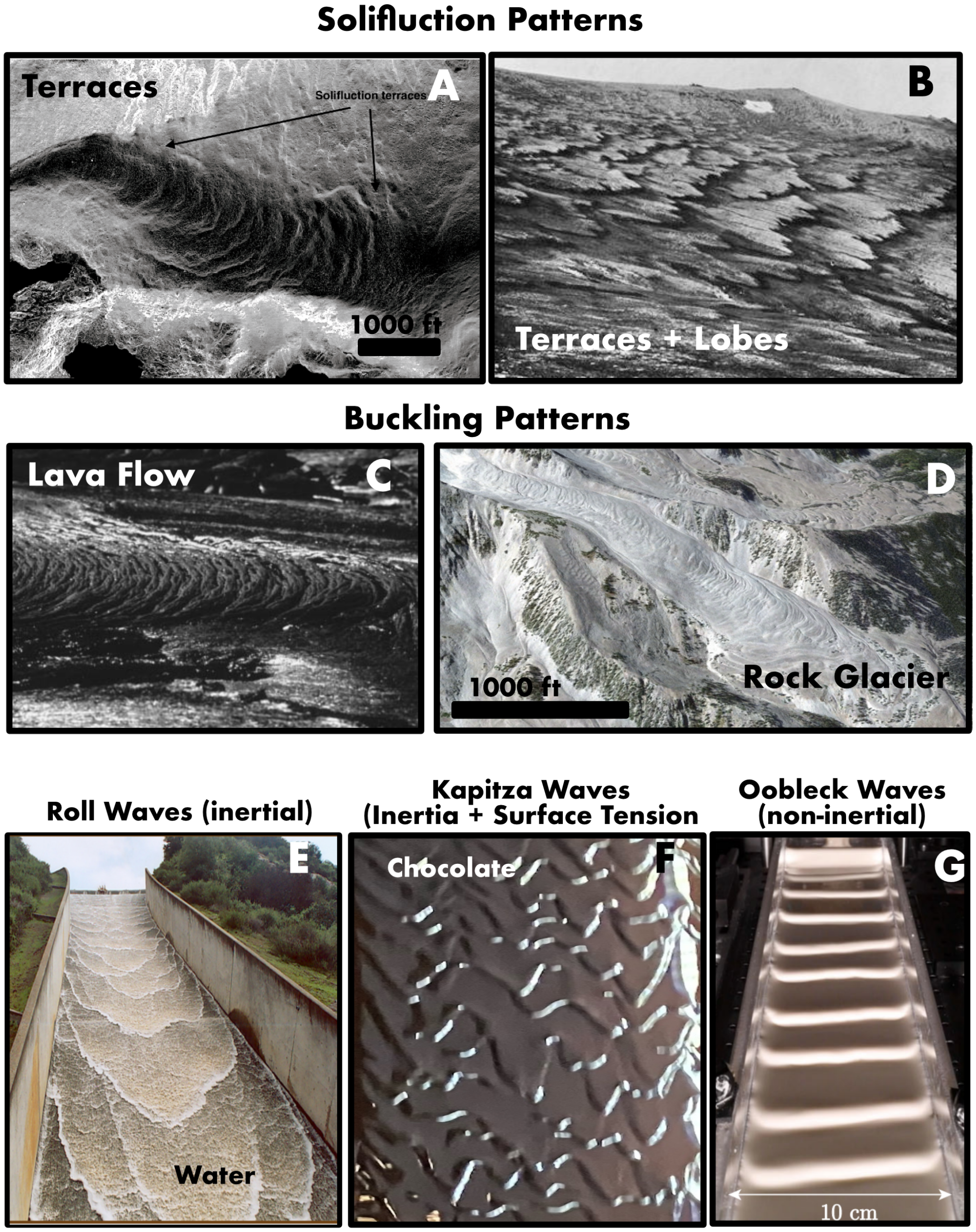

Figure 1: **Photos of solifluction terraces and possible analogues explored in this paper.** (**A**) LiDAR-derived slope map of solifluction terraces at Niwot Ridge, Colorado. (**B**) Solifluction patterns in Chicken Creek, AK. Photo by Philip S. Smith. (**C**) Buckling of a lava flow, from (*22*). (**D**) Buckling on a rock glacier at Mt. Sopris, Colorado. From Google Earth. (**E**) Inertial roll waves at Turner reservoir, CA. Photo by Victor Ponce.(**F**) Kapitza waves in a chocolate waterfall. Photo by Chloe Lindeman. (**G**) Non-inertial experimental oobleck waves, from (*23*).

of solifluction lobe wavelength and morphology using a large dataset from Norway (*4*). Another recent study found similar scaling in lobate patterns on Mars, suggesting similar formational mechanisms (*14*). These first-order scaling analyses have the advantage of being largely insensitive to rheology; however, they cannot predict the onset of the instability or provide a detailed physical model of soil motion. Further, these studies did not identify a particular mechanism of stalling at lobe fronts, and did not attempt to explain the primary instability of terrace formation.

Inspired by this and recent studies in non-Newtonian fluids, here we use a combination of scaling analysis, linear stability analysis, remote sensing and a broad review of literature from different fields to explore different possible mechanisms for the formation of solifluction terraces. Perhaps most importantly, our work demonstrates which simple models (frost heave + fluid-like flow) and potentially analogous systems (buckling instabilities, roll waves) are *not* able to explain the formation of solifluction terraces, while using recent findings in soft matter physics (oobleck waves) to develop a new qualitative conceptual model for solifluction patterns, highlighting possible mechanisms for the onset of non-inertial instabilities and suggesting future field and experimental work. Our proposed model may explain both terraces and lobes, as both instabilities likely require similar behavior focused at soil fronts. We also discuss potential reasons why these patterns are only found in cold landscapes, despite the fact that soil creeps downhill due to gravity and disturbance in every climate zone (*25, 26*). Our study can be viewed as a thought paper that synthesizes a number of competing hypotheses for solifluction pattern formation, pointing the way forward for future field, experimental, and theoretical work on this rich problem.

Section 2 discusses what we know about solifluction processes, including field and lab measurements of solifluction motions that ground our theoretical discussion in real data. Section 3 examines the possibility that solifluction terraces are an example of a buckling instability. Section 4 uses a simple fluid scaling analysis to explore wavelength scaling with soil thickness and slope in remote sensing data from Norway. Section 5 introduces the concept of linear stability analysis by evaluating the stability of our simple fluid formulation. Section 6 evaluates the stability of a more complex formulation that reproduces the vertical velocity profiles observed in the field. Section 7 evaluates the stability of a formulation inspired by oobleck waves, in which viscosity increases at the front of bumps. Section 8 presents our conceptual model inspired by our analysis, highlighting the necessary and sufficient ingredients to produce solifluction patterns. Section 9 discusses the many limitations of our study and open questions that deserve further study.

2 Solifluction Processes

While solifluction processes and rates have been documented in the field for over a century (*8*), due to the complexity of the temporally evolving soil/ice/water mixture, a straightforward description of the rheology of solifluction soil remains out of reach. During fall freeze up, ice lenses form in the soil as supercooled water migrates along grain boundaries and self organizes into discrete lenses of ice (*6, 7, 27*) (while this fascinating and complex phenomenon deserves further consideration, a complete review of the relevant literature is outside the scope of this study). This leads to frost heave, which lofts soil upwards during fall freeze-up. One common misconception is that frost heave occurs only due to the volumetric expansion of water as it turns to ice; however, in the presence of ice lenses water migrates from the pore space to discrete lenses, resulting in frost heave of up to tens of centimeters at the surface—far surpassing simple expansion due to the volume change of water to ice, which can only cause a 9% change in volume of the soil column (*6*). During the winter, presumably little to no motion occurs in the soil (though direct observation of soil motions are challenging under the snowpack). In the summer, thaw begins from the top down, causing 1) frost creep due to thaw consolidation vertically downward and 2) saturation and subsequent "flow" of the soil (*8*), known as "gelifluction" (Fig 2B) and 3) sometimes, retrograde motion uphill, thought to be due to cohesive effects (*3*). Frost creep can be conceptualized as the lofting of soil along a direction normal to the slope, driven by ice lens formation during freeze events, followed by vertical settling upon thaw (Fig 2B). With this conceptual model in mind, (*8*) use a simple geometric frost heave and settling model to define event-scale frost creep flux as:

$$q_i = -\frac{\rho_b \beta}{2} \frac{d\zeta}{dx} d_f^2 \tag{1}$$

where ρ_b is the bulk density of the soil, β is the soil strain upon freezing, $d\zeta/dx$ is the surface slope, and d_f is the penetration depth of a particular frost event. (*8*) point out that this is akin to a diffusive flux commonly used for hillslope sediment transport , albeit one that acknowledges the processes that contribute to the diffusivity. Note that we use the convention of positive flux downhill in the positive x direction, leading to the negative sign in 1.

Using a plausible distribution of frost penetration depths that falls off exponentially with depth into the soil—that is, shallower frost penetration depths are far more likely than deeper ones and depend on climate—the annual frost creep flux (M/LT) becomes:

$$Q = \frac{-\rho_b \beta f}{2} d_{f*}^2 \frac{\partial \zeta}{\partial x} \tag{2}$$

where d_{f*} is the mean annual frost penetration depth and f is the number of frost events per year. While this example of a classic diffusive flux may be useful for larger timescales of landscape evolution, it is clear that due to the incredible stability and smoothing behavior of diffusion processes, it is unlikely that they will be able to produce solifluction instabilities. Further, the morphology of solifluction lobes and terraces points toward a more complex story in which soil can maintain very steep–even past vertical–fronts, precluding a simple diffusive-like process (Fig2A). Solifluction consists of not only frost creep , but also gelifluction, or the fluid-like motion of soil upon spring thaw (*10*). Though little is known about gelifluction dynamics, it is likely an important piece of the puzzle.

2.1 Field and Lab Measurements of Solifluction Motions

Solifluction motions are typically measured with markers placed either at the surface of the soil or a series of dowel rods placed at depth and dug up the following year to measure vertical displacement profiles, both in the field (e.g., (*28–34*)) and in laboratory experiments (*10, 35*). While the shape of these profiles can vary from concave up to concave downward, the majority display exponential (concave down) profiles that exhibit the largest displacement at the surface, falling off exponentially with depth up to about 1 meter (Fig 2C; (*4*)). In a typical fluid flow, the vertical velocity profile may be used to understand the rheology of the fluid (the relationship between shear stress and strain rate). However, the difficulty in solifluction lies in the fact that velocities are so slow that vertical profiles are actually displacement, not velocity, profiles. Because thaw occurs from the top down, field measurements show not the instantaneous velocity of the soil but the time integrated displacement; thus the question remains, does the soil show an exponential profile due to its unique rheology, or simply because the top thaws first? One study used a string of strain gauges to obtain shorter timescale velocities of soil displacement and found a linear velocity profile with depth (*36*);

this suggests a simple summation of frost heave displacement over time as the thaw front propagates downward. A more recent study (*37*) using high precision accelerometers measured complex vertical velocity profiles that are exponential (concave down) at depth and concave up at the surface. These complex velocity profiles are similar to those seen in dense granular flows, where a rapidly moving surface layer overlies a slowly creeping subsurface (e.g., (*38*)). However, given the exceedingly slow velocities of soil motions, it is unlikely that surface motion would meet the criteria for "flow" as typically conceptualized in granular physics; a more soil mechanics-based formulation may be relevant, and one of the few experimental studies of solifluction found that gelifluction likely has a plastic creep, rather than time dependent viscous, rheology (*19*).

In addition to measurements of vertical displacement in the soil column, a few studies have observed differences in surface velocities across individual solifluction lobes. In a comprehensive mapping of solifluction features in Niwot, Colorado, (*39*) observed that surface soil velocities on a solifluction lobe increase toward the steep front, where they quickly drop off to the lowest velocities on the lobe (Fig2D) resulting in a buildup at the front. The directions of velocity vectors resemble what might be expected in a fluid flow, where soil is focused into the lobe and then diverges at the lobe front. The buildup at the front of solifluction lobes has been observed with more modern monitoring efforts, including repeat drone photogrammetry (*40*). While physical mechanisms for this buildup at the front are unknown, patterns of soil moisture, vegetation growth, and compaction may be important (*17, 39, 40*). In this study we will ultimately argue that heterogeneities in velocity across bumps in surface topography, rather than inherent details of rheology, drive the formation of solifluction patterns (spoiler alert!).

3 The Allure of Visual Similarity: Buckling Instabilities and Roll Waves

Here we explore possible connections between solifluction terrace patterns and two visually similar fluid patterns. At first glance, solifluction terraces bear a striking resemblance to buckling instabilities (Figure 1). This led us down an immense rabbit hole of literature spanning multiple disciplines. Soft materials, including thin elastic sheets and thin film fluids, commonly undergo buckling insta-

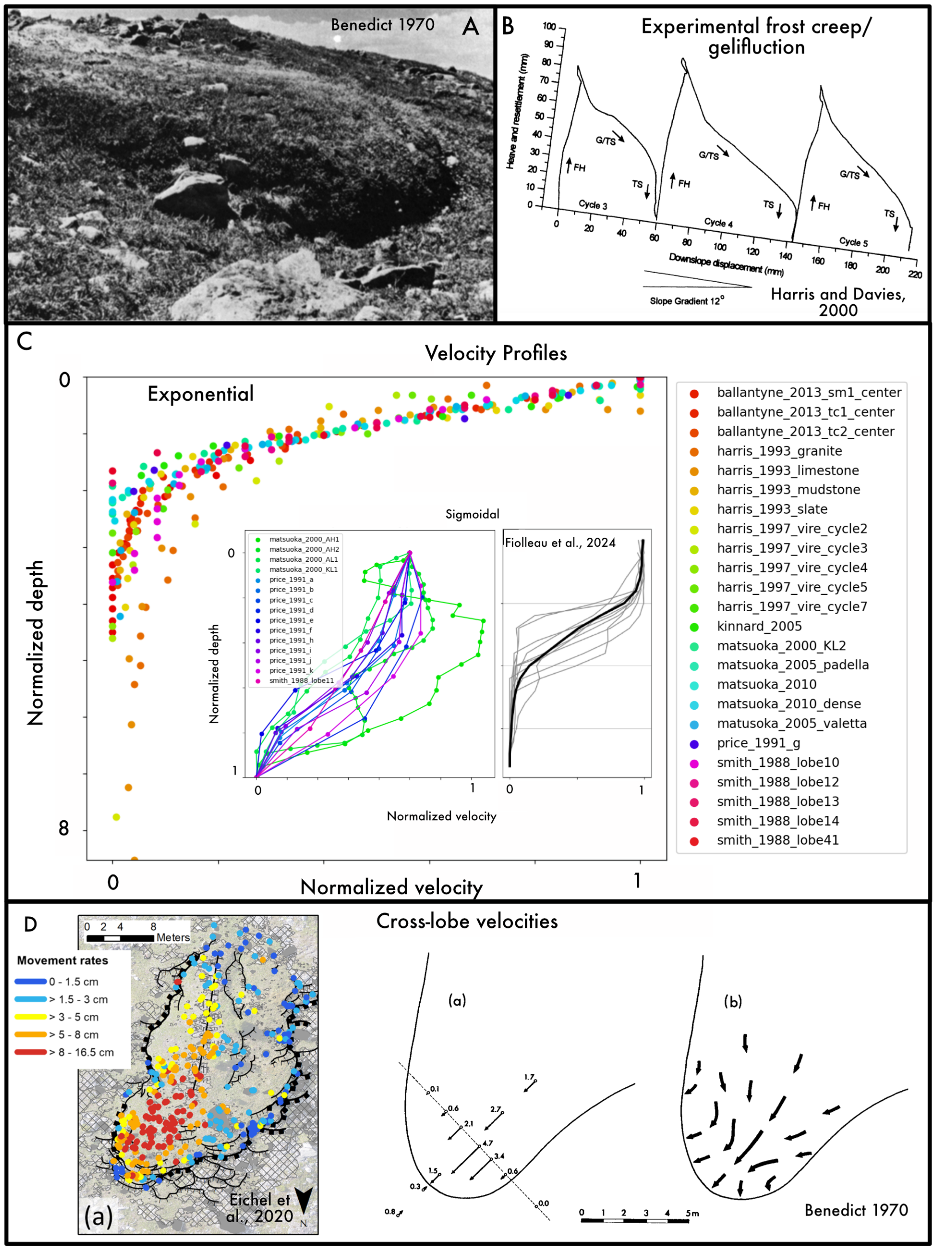

Figure 2: **Field data illustrating soliflucting soil motions**. (**A**) Photo of a solifluction lobe from Niwot Ridge, CO illustrating steep, overhanging front (photo from (*39*)). (**B**) Experimental solifluction displacements reprinted from (*10*) illustrating frost heave (FS), gelifluction (G), and thaw consolidation (TS) over three cycles of freeze thaw. (**C**) Time-averaged velocity profiles compiled from the literature show highest velocity at the surface. While most profiles are exponential with depth, faster soil velocities result in a sigmoidal profile (insets). (**D**) Field measurements of differences in soil velocity across solifluction lobes. Left: drone photogrammetry-derived soil movement rates (cm/yr) from (*40*)). Right: Soil velocity measurements in cm/yr from (*39*)).

bilities in which the material self-organizes to compress and form folds or buckles (Figure 1C,D). Buckling has been shown to occur at a variety of length and time scales in both geological processes and everyday materials due to 1) compression (e.g., ice sheets (*41*), rock folds (*42*), buckling of subducted lithospheric plates (*43*), buckling of elastic plates (*44*), coiling of honey (*45*) and/or 2) strain mismatch between different layers of fluid or soft materials, particularly where a resistant layer overlies a more deformable layer (e.g., transverse ridges in rock glaciers (*46*), lava flows (*22*), an elastic sheet overlying a shear fluid (*47*), growth-induced instabilities in multilayer materials, like pumpkins or shar pei dogs (*48*)) (see (*47*) for a nice brief review of the literature).

Compression buckles can occur all at once in a material compressed from both sides (e.g., (*42*)) or will occur in succession for a material undergoing compression from one side (e.g., (*43, 49–51*), as can be observed when pouring cake batter into a pan. While the mechanism is similar in all cases of compression buckling, the governing equations and therefore stability criteria and wavelength predictions are unique to the specific geometry and materials for each case. (*42*) first studied folding in viscoelastic rock layers embedded within rocks of different effective viscosities when compressed from both sides, finding that wavelengths tend to be on order of 20-50 times the thickness of the layer, depending on the viscosity contrast. (*52*) found that rock layers oblique to the axis of principal compression behave similarly. Periodic folding of a vertically falling viscous sheet (*49*) exhibits wavelengths primarily dependent on the fall velocity and sheet thickness, with relevance not only for pouring fluids like honey, but also for subducting plates (*43*). (*41*) found that buckling of ice sheets depends only on the compressional pressure in the ice, not on ice thickness.

In a large dataset of solifluction terraces in Norway, wavelength to soil thickness ratios range from 10-70 (*4*) (Figure 3B), not dissimilar from ratios found in folding under compression (*42*). While hillslopes are unlikely to be compressed on both top and bottom, it is plausible that soil creeping down a concave up slope may experience compression at the base of the slope. If this were the case, we might expect that most solifluction terraces form on concave-up slopes where compression may occur at the base. However, profiles of terraced slopes across Norway demonstrate that solifluction terraces can form on slopes of any curvature (Figure 3) (see (*4*) (*?*)). It is possible that some of these are paleoterraces developed at a time when hillslope curvature was different. However, the morphology of solifluction terraces is also strikingly different from that of compression buckles; wavelengths are quite large, on order of tens of meters, and terraces gently grade into a

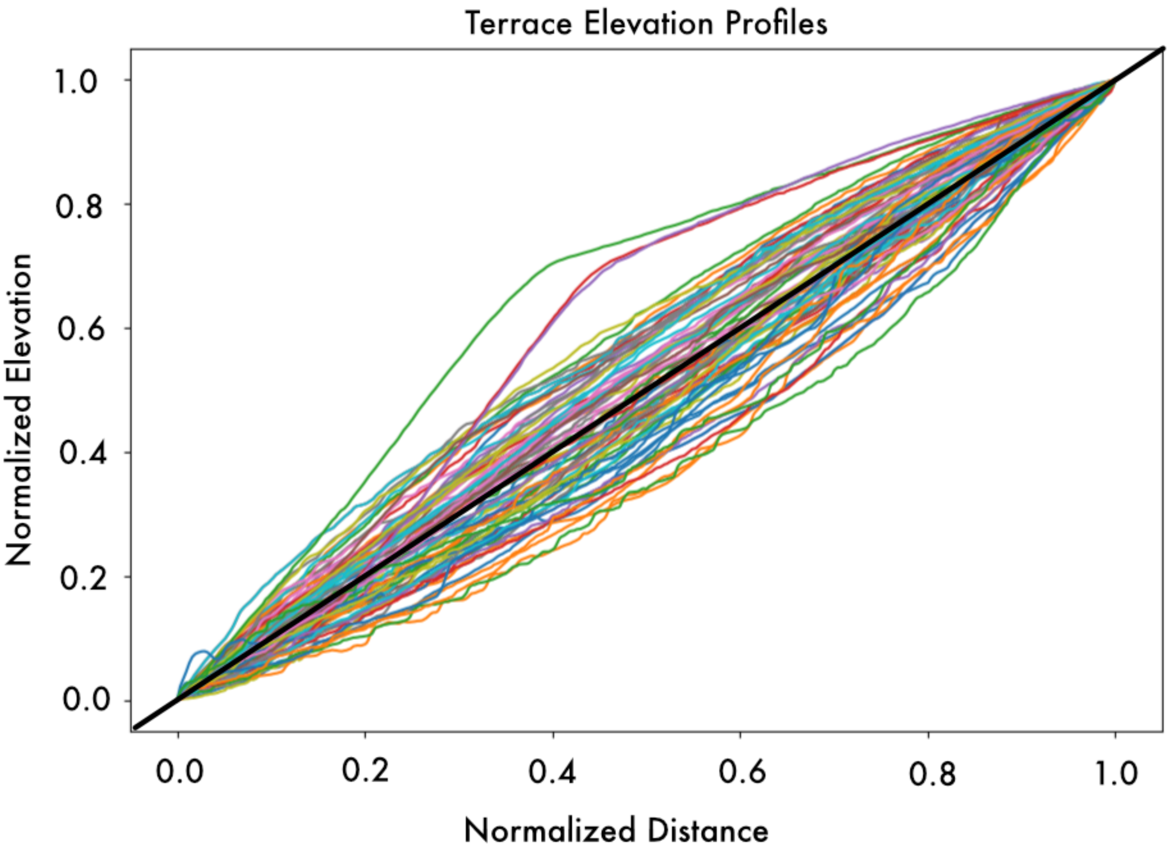

Figure 3: **Downslope elevation profiles of sites with solifluction terraces**, normalized by max and min elevation and distance. Note the wide variety of profiles curvatures- many terraces occur on convex-up slopes, bringing into question the argument that terraces form due to compressional buckling. Different colors only help the eye to differentiate individual profiles.

steep front, rather than demonstrating symmetrical periodic folds typical of the settings mentioned above. While the compression buckling mechanism is unlikely, a good field test could be done in which terraces are radiometrically dated (e.g., (*53*)). If compression buckling were indeed the mechanism for the instability, we would expect to see progressively younger terraces moving from the bottom to the top of the slope. Note that we do see smaller scale "rumples" or buckles at the toe of active layer detachments and earthflows that are good candidates for compression buckling (*54*).

The second common buckling mechanism involving strain mismatch between different layers, particularly with a viscous fluid or elastic sheet riding atop a less viscous fluid, could be relevant for solifluctING soil. This situation results in folds that strongly resemble solifluction terraces (Figure

1C,D). Does soliflucting soil contain multiple layers that could allow for this mechanism to occur? At first glance, it seems that the surface layer of vegetation could induce buckling, much like the crust at the surface of a lava flow produces folds (*55*), or the debris on top of a rock glacier produces ridges (*46*) at large wavlengths (tens of meters) that are comparable to solifluction terrace wavelengths. These studies find that buckling wavelength is primarily a function of the thickness and rigidity of the surface layer, with a wavelength roughly an order of magnitude larger than the thickness of that layer (*46*) however, typical tundra vegetation layers are on order of 10cm, much too small to explain wavelengths on order of tens or hundreds of meters (Figure 1A; Figure 4). It is possible that soil moisture or ice conditions lead to a thicker drier ”skin” at the surface of the soil with higher effective viscosity. However, vertical displacement profiles of soliflucting soil show little to no decrease in velocity at the surface; in fact, there is a marked increase in velocity at the surface (Figure 2C), presenting a strong argument against a multilayer buckling mechanism.

Another strikingly similar instability (Fig1E, F) occurs when a thin layer of fluid flowing down a plane produces self-organized patterns known as roll waves or Kapitza waves (*56*) (notably, this seminal study was conducted by father and son team while on political house arrest in Soviet Russia (*57*). Roll waves can be seen in rainwater flowing down a street, or in the sheets of water cascading down a waterfall. They can also be observed in granular suspensions such as mudflows (*58*). These instabilities occur when infinitesimal perturbations in flow thickness become unstable and grow as thicker flow moves faster. Roll waves probably most closely resemble the morphology of solifluction waves, with the ability to form both downslope and cross-slope waves that override each other and coalesce (Fig 1F). However, there is a key requirement for the initiation of roll waves that is conspicuously missing in solifluction: inertia. In Newtonian flows, a critical finite Reynolds Number $Re = \rho UL/\mu$ —typically on order of 10 or greater—is required for onset of roll waves (*59*). While less is known about roll waves in non-Newtonian flows, they have also been shown to exhibit a critical Re greater than 1 (*58, 60*). Assuming an effective viscosity of $10^5 - 10^{12}$ Pa-s (*4*), with velocities on order of 1cm/yr and a length scale of a meter, Reynolds numbers in soliflucting soil could be as low as 10^{-22}: unquestionably non-inertial. We can also evaluate the inertia of our system a different way with the inertial number $I = \dot{\gamma} d/\sqrt{P/\rho_p}$ from granular physics (*61*), where $\dot{\gamma}$ is the shear rate, d is the particle diameter, P is the pressure and ρ is the density of the particles. Using a characteristic shear rate of $10^{-9}/s$ from vertical displacement profiles observed in the field (Figure 2C; Supplementary Materials), a characteristic particle size of .01mm (silt), a pressure $P = \rho_b g H \approx (1500 kg/m^3)(9.8 m/s^2)(1m) \approx 15000 Pa$, and particle density of $2650 kg/m^3$, we estimate $I \approx 10^{-18}$. This is many orders of magnitude below the threshold $I \approx 10^{-3}$ for quasistatic (i.e., non-inertial) flow, as expected for slowly creeping soils (*21*). Thus, mechanisms for the onset of solifluction instabilities must not rely on the presence of inertia. We formally show the unconditional stability of a simple non-inertial fluid flow in section 5.1. We conclude that solifluction terraces sadly cannot be explained by alluringly simple direct analogies to fluid buckling or roll wave instabilities.

4 Scaling Analysis for Solifluction Terraces

We now seek an explanation for solifluction terraces that does not rely on the presence of multiple layers, compression, or inertia. Here we develop a series of simple theoretical formulations to explore other possible mechanics for the onset of solifluction instabilities. Given 1) the similarities between solifluction patterns and fluid instabilities (*4*), 2) the complexity and uncertainty of solifluction rheology, and 3) the general fluid-like behavior of soft matter including earth materials (*21*), for simplicity we ground our formulations in the language of fluid mechanics; however, we emphasize that future work could (and should) explore similar formulations in the realm of granular physics, soil mechanics, and even stastistical physics that acknowledges the stochastic and possibly non-continuum nature of seasonal soil motions (*62*).

In this section we present a scaling analysis for a simple fluid flowing down an inclined plane in an effort to predict the wavelength scaling for solifluction terraces. In the case of solifluction, the “fluid” is mobile soil and the inclined plane is either bedrock or an immobile permafrost layer. Note that this approach follows directly from that of (*4*) for the cross-slope patterns of solifluction lobes, but ignores any dynamics in the cross-slope direction to focus on dynamics in the downslope (x) direction. Because the rheology of soliflucting soil is unknown, we begin with a simple fluid rheology that includes the role of hydrostatic pressure, and see that similar to findings in (*4*) for cross-slope patterns, the resulting first-order scaling, though noisy, generally agrees with measurements of downslope solifluction terrace wavelengths from remote sensing imagery in Norway. While this alone does *not* prove that soliflucting soil behaves as a simple fluid, it importantly offers *support* for a first-order fluid-like behavior that cannot be disproved by our data. Any fluid-like material (even with complex non-Newtonian rheology) should obey scaling similar to what we find here.

We then present a linear stability analysis, illustrating that our simple choice of non-inertial governing equation with Newtonian rheology is unconditionally stable and therefore not sufficient to explain the onset of the solifluction terrace instability. However, to be clear, this does not invalidate the utility of the scaling analysis, which simply predicts scaling and not a preferred wavelength or conditions for the instability. In subsequent sections we explore more complex formulations of the problem.

4.1 1D scaling analysis for a simple fluid

This and all the following analyses begin with the setup of fluid flow with vertical thickness H on an inclined plane. Assuming a simple non-inertial fluid-like rheology for soil transport, we define the basal shear stress as:

$$\tau_{0x} = \rho g H S - \rho g H \frac{\partial H}{\partial x} \tag{3}$$

where ρ is the bulk density of soil, g is gravitational acceleration, H is the soil thickness, and S is the topographic slope $\sin\theta$, and x is the horizontal component (defined as increasing downhill). The first term on the right hand side is the shear stress due to the overlying weight of the soil on an inclined plane, while the second term is the hydrostatic pressure resulting from bumps in the topography. Because we do not know the precise rheology of solifluctING soil, we define a bulk dynamic viscosity μ such that:

$$\tau_{0x} = \mu \frac{U}{H} \tag{4}$$

where U is the vertically-averaged velocity in the downslope (x) direction. Setting 3 equal to 4 we find:

$$U(x) = \frac{\rho g H^2}{\mu}\left(S - \frac{\partial H}{\partial x}\right) \tag{5}$$

According to continuity:

$$\frac{\partial H}{\partial t} + \frac{\partial q_x}{\partial x} = 0 \tag{6}$$

where t is time and $q_x = HU$ is the flux. Evaluating $\frac{\partial q_x}{\partial x}$ and plugging into 6, we find:

$$\frac{\partial H}{\partial t} + \frac{\rho g}{\mu}\left[3H^2 S\frac{\partial H}{\partial x} - 3H^2\left(\frac{\partial H}{\partial x}\right)^2 - H^3\frac{\partial^2 H}{\partial x^2}\right] = 0 \tag{7}$$

Assuming the local term is negligible near a flow front and terms that contain products of derivatives are small compared to the other terms, we find:

$$0 = 3S\frac{\partial H}{\partial x} - H\frac{\partial^2 H}{\partial x^2} \tag{8}$$

Now we non-dimensionalize terms such that:

$$\begin{aligned} x &= \hat{\lambda}\lambda, \\ H &= \hat{H}H_0 \end{aligned} \tag{9}$$

where H_0 is a characteristic soil thickness and λ is a characteristic length in the x direction. Substituting these into 8 yields:

$$3S\frac{H_0}{\lambda}\frac{\partial \hat{H}}{\partial \hat{\lambda}} - \frac{H_0^2\hat{H}}{\lambda^2}\frac{\partial^2 \hat{H}}{\partial \hat{\lambda}^2} = 0 \tag{10}$$

Simplifying and retaining only the dimensional coefficients, we find:

$$\lambda_d \sim \frac{H_0}{3S} \tag{11}$$

(we rewrite λ as λ_d here, under the assumption that λ relates to the downslope wavelength of solifluction terraces). Eq. 11 suggests that terrace wavelength should scale linearly with soil thickness divided by topographic slope, where thicker soil or shallower slopes result in larger downslope wavelengths. The factor of 3 in the denominator may not be meaningful, as a full solution would likely include an additional constant. Scaling is a first order analysis that is largely insensitive to the complexities of rheology. To be clear, the scaling seen in 11 can be viewed as a minimum requirement for a system to be considered fluid-like; however, agreement with that scaling does not “prove” in any way that we have the proper governing equations for our system.

4.2 Solifluction Terrace Scaling from Remote Sensing Data

To determine whether this simple scaling agrees with observations, we use a high resolution dataset from Norway (*4*) to measure downslope solifluction terrace wavelength γ, height h, and topographic slope S. Note that measured terrace height h is different from the initial height h_0 at the onset of the instability, adding a source of error. While limited data prevent us from confidently determining the scaling relationship, results show that terrace wavelength increases and may generally scale linearly with h/S, with a large amount of scatter characteristic of remotely sensed data of subtle topographic features. Each data point in Figure 4 represents an average of wavelength, height and slope values from a single transect including multiple terraces taken from 30 different sites across Norway (see (*4*) and (*?*)). Vertical and horizontal lines represent standard error. Similar to (*4*), because scaling is typically not sensitive to details of rheology, this scaling solifluction patterns may generally obey fluid-like behavior. More cautiously, this scaling shows that solifluction patterns don't *not* obey fluid-like behavior. As discussed in the following sections, a better understanding of the rheology and other phenomenological aspects on the system are needed to predict the onset of the instability. See (*4*) for detailed remote sensing methods.

5 Evaluating Stability of Potential Solifluction Formulations

Here we turn to a series of linear stability analyses to determine the stability of different fluid-like formulations to infinitesimal perturbations. First, we show that a stability analysis for our simple fluid formulation (Eqn. 5) is unconditionally stable, and thus likely unable to explain the onset of the instability. In the following sections we build complexity to determine what general type of formulation may ultimately be able to explain solifluction patterns. We also emphasize that a key aim of this study is to clearly explain why linear stability analysis is useful and to demonstrate how to conduct one for readers who may not be familiar with the technique.

5.1 Linear Stability Analysis for a Simple Fluid

Here we use linear stability analysis to formally demonstrate the stability of the above formulation for non-inertial flow, thus showing that solifluction terraces cannot be produced from the same

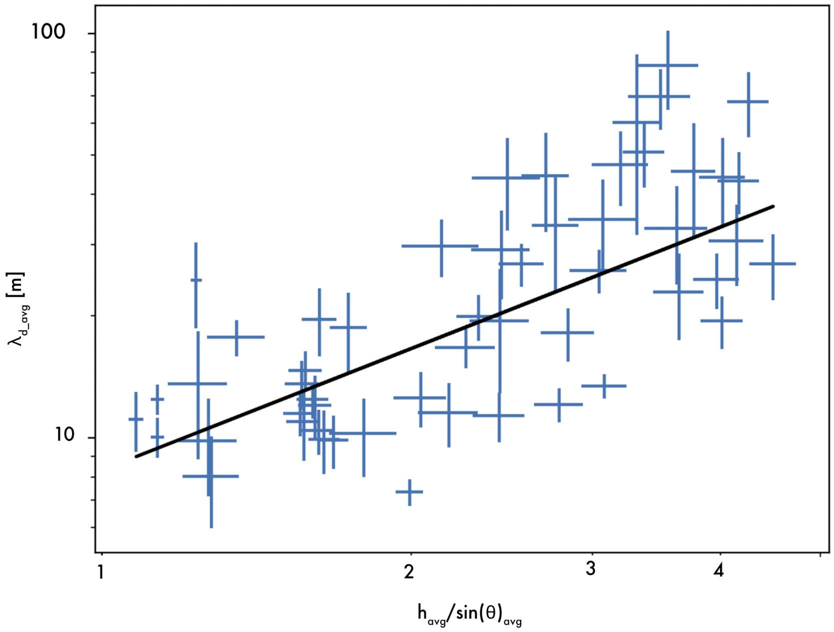

Figure 4: **Scaling between downslope terrace wavelength, height and slope for from a large dataset in Norway** (*4*). Each point represents the mean wavelength, height and slope from a given downslope-oriented transect. Vertical and horizontal lines represent standard error. Black line is the theoretical curve from our scaling analysis.

instability as roll waves. We fully outline each step of the stability analysis in an effort to be accessible to readers who are not familiar with this technique. Subsequent stability analyses in this paper will be presented in shorter form with detailed analysis in Supplementary Materials. Essentially, a linear stability analysis explores the initial stability of an equation or set of equations when subjected to an infinitesimal perturbation around a base state. It is important to note that more complex nonlinear stability analyses (not attempted in this study) or numerical solutions are required to predict more complex behavior after the onset of the instability, nonlinear effects, or instabilities that require a finite amplitude initial perturbation (see example in Section 7.1).

Beginning with Eqn. 7 and ignoring the second term on the RHS that contains products of derivatives because they don't contribute first order terms, we have:

$$\frac{\partial H}{\partial t} + \frac{\rho g}{\mu}\left[3H^2 S\frac{\partial H}{\partial x} - H^3\frac{\partial^2 H}{\partial x^2}\right] = 0 \tag{12}$$

Now we allow for a small perturbation to the soil depth H:

$$H(x,t) = H_0 + H_1(x,t) \tag{13}$$

where H_0 is the base state with uniform flow thickness, and H_1 is a first-order perturbation around this base state. Substituting Eqn. 13 into Eqn. 12, we have:

$$\frac{\partial(H_0 + H_1)}{\partial t} + \frac{\rho g}{\mu}\left[3(H_0 + H_1)^2 S \frac{\partial(H_0 + H_1)}{\partial x} - H^3 \frac{\partial^2(H_0 + H_1)}{\partial x^2}\right] = 0 \tag{14}$$

Note that H_0 is constant and therefore does not change with time or space, so can be removed from the derivatives. Expanding the parenthetical terms, this leaves us with:

$$\frac{\partial H_1}{\partial t} + \frac{3\rho g S}{\mu}(H_0^2 + 2H_0H_1 + H_1^2)\frac{\partial H_1}{\partial x} - \frac{\rho g}{\mu}(H_0^3 + 3H_0^2H_1 + 3H_0H_1^2 + H_1^2)\frac{\partial^2 H_1}{\partial x^2} = 0 \tag{15}$$

Retaining only the terms that are linear in H_1 leaves with us the linearized governing equation:

$$\frac{\partial H_1}{\partial t} + \left(\frac{3\rho g S H_0^2}{\mu}\right)\frac{\partial H_1}{\partial x} - \left(\frac{\rho g H_0^3}{\mu}\right)\frac{\partial^2 H_1}{\partial x^2} = 0 \tag{16}$$

Now to do the stability analysis we assume a solution (*63*) of the form:

$$H_1(x,t) = A_0 e^{\gamma t + ikx} \tag{17}$$

where A_0 is the initial amplitude, $k = 2\pi/\lambda$ is the wavenumber (where λ is the wavelength), and γ is a complex number where the real part represents the growth rate and the imaginary part represents the celerity of the waveform. For reference, the relevant derivatives are:

$$\frac{\partial H_1}{\partial x} = A_0 ik e^{\gamma t + ikx} \tag{18}$$

$$\frac{\partial^2 H_1}{\partial x^2} = -A_0 k^2 e^{\gamma t + ikx} \tag{19}$$

$$\frac{\partial H_1}{\partial t} = A_0 \gamma e^{\gamma t + ikx} \tag{20}$$

Substituting these into Eqn. 16 and simplfying, then solving for γ, we find:

$$\gamma = -\frac{\rho g H_0^3}{\mu} k^2 - i \frac{3\rho g S H_0^2}{\mu} k \tag{21}$$

The sign of the real part of the growth rate σ determines the stability of the system; positive growth rate indicates instability, while negative growth rate indicates stability. In our case, the real part of the growth rate is negative for all values of k, which means that the equation is unconditionally stable. The waveform decays to its base state with a rate that increases nonlinearly with k. The imaginary term is also negative for all k, representing a negative phase for a positive waveform celerity such that short wavelengths travel downstream faster than large wavelengths. In a more interesting result, we might find conditional stability such that the system becomes unstable for only certain values of k. In that case, stability analysis can often be used to determine the wavenumber associated with the maximum growth rate, which gives a prediction of the preferred wavelength of the instability (*64*). Our finding of unconditional stability for our simple fluid formulation most likely means that our chosen governing equations are not sufficient to explain the observed instability. Additionally, linear stability analysis only examines stability in the face of an infinitesimal perturbation; some systems may require a finite amplitude A_0 in order to become unstable. It is possible that the real instability is nonlinear, thus requiring a trickier nonlinear stability analysis (however, numerical solutions can always help determine stability (see Section 7.1)). However, we have good reason to believe that our governing equations are simply not sufficient, given the complex rheology and natural heterogeneity of soliflucting soil. We explore this in the following sections.

6 Stability analysis for exponentially increasing viscosity with depth

The fluid formulation presented thus far is highly simplistic and therefore is not able to produce complex vertical velocities profiles observed in the field and lab (Fig 2). Here we add an element of complexity and allow effective viscosity to increase with depth into the soil column, as proposed in (*4*) and detailed in section 2.2. We note that this approach is similar to granular formulations like $\mu(I)$ (*65*), though there are two challenges with directly applying $\mu(I)$ to our system: 1) we lack an understanding of how μ changes with depth and 2) our slow, sub-yield soil motions may not be valid for $\mu(I)$ (*21*). Therefore, for simplicity, here we use a very simple fluid formulation with viscosity increasing with depth to explore how rheology may affect pattern formation, acknowledging that we still lack a comprehensive set of governing equations for our system.

Let's assume a simplified formulation for effective viscosity in which viscosity μ exponentially increases with depth into the soil, beginning with a constant viscosity μ_0 at the surface:

$$\mu(z) = \mu_0 e^{a(H-z)} \tag{22}$$

where z=0 at the base of the soil column and z=H at the surface. Following the same approach in section 4.1 and using a no slip boundary condition at the base of the soil column were z=0 (Supplementary Materials), we can solve for the x-directed vertical velocity profile as:

$$u(z) = \frac{\rho g(s - \frac{\partial H}{\partial x})}{\mu_0} \left[\frac{e^{a(z-H)}(a(H-z)+1}{a^2} - \frac{e^{-aH}(aH+1)}{a^2} \right] \tag{23}$$

Note that for this equation to be valid, $0 < z < h$, and $a > 0$ (i.e., viscosity increases with depth). With the assumption of Eqn. 22 as a viscosity formulation, this expression nicely captures the range of behavior seen in field and lab measurements (Fig. 2, 5). For small a, viscosity increases slowly with depth and the velocity profile resembles that of a typical fluid. For intermediate a, the velocity profile exhibits an exponential shape at depth, transitioning to a fluid-like shape at the surface. For high a, the profile is largely exponential, with the exception of a tiny fluid-like zone at the surface (fig 5).

We can perform a linear stability analysis to evaluate whether a formulation of this type could produce an instability leading to the patterns we observe. Following the process detailed in section 5.1, with some unpleasant algebra (Supplementary Materials), we find:

$$\gamma = \left[\frac{2\rho g(e^{-aH_0} - 1)}{\mu_0 a^3} + \frac{2\rho g h_0 e^{-aH_0}}{\mu_0 a^2} + \frac{\rho g H_0^2 e^{-ah_0}}{\mu_0 a} \right] k^2 - \left(\frac{\rho g s H_0^2 e^{-aH_0}}{\mu_0} \right) ik \tag{24}$$

It can be shown that if $(\rho, g, \mu_0, a, H_0) > 0$, then the real part of the growth rate is unconditionally stable (Supplementary Materials). Thus, even though this formulation captures the observed velocity

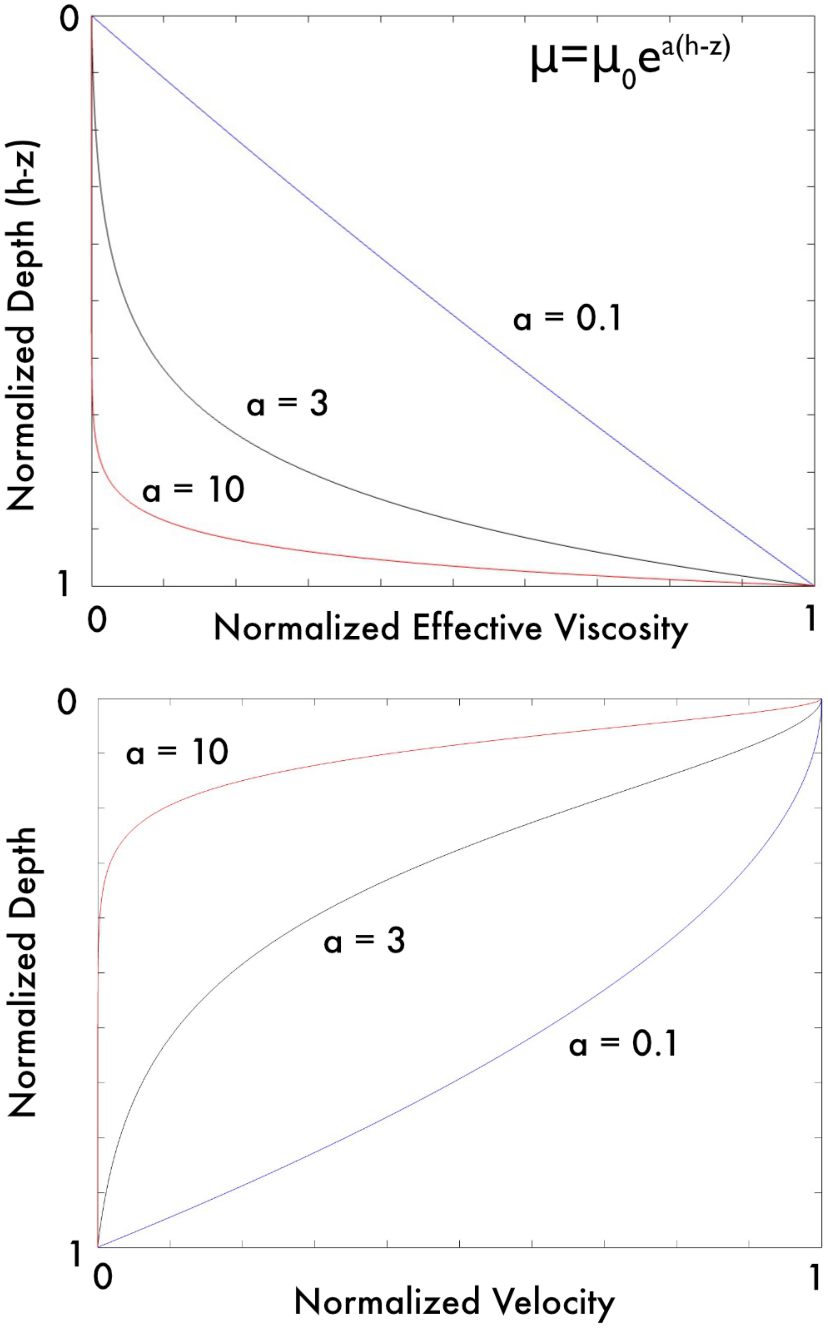

Figure 5: **Example normalized vertical profiles** of A) viscosity (Eq. 22) and B) velocity (Eq.23) with depth for different values of scaling factor a.

profiles and moves beyond a simple Newtonian fluid, it is unfortunately not enough to explain the onset of these patterns. We are still missing some important element of the problem.

7 Bump-Dependent Viscosity Inspired by Oobleck Waves

So far we have discounted many proposed mechanisms of solifluction instability including simple frost creep, buckling instabilities that require compression or multilayers, roll wave instabilities that require inertia, and a depth-dependent viscosity formulation. What are we left with? A pair of recent studies has identified a new type of wave-like instability that can occur in non-inertial flows. Dubbed ”oobleck waves” (Figure 1G), this instability is thought to occur due to the unique S-shaped rheological curve of certain shear-thickening fluids such as oobleck (cornstarch mixed with water) (*23, 66*). The S-shape of the rheological curve refers to a region where, at high volume fractions (%solid/%liquid), the strain rate bizarrely decreases as the shear stress increases. This can be thought of as a stress-dependent viscosity, where viscosity increases as stress increases. In the presence of a bump, higher stress on the downhill side of the bump increases viscosity there, leading to a growth of the bump (*23*). Linear stability analysis shows that this formulation leads to unconditional instability (*66*) and provides a non-inertial mechanism for wave-like instabilities at very low Reynolds Number that doesn’t rely on external compression or the presence of multiple layers as in buckling instabilities.

Could a similar mechanism be happening with solifluction? Looking at vertical displacement profiles, their exponential shape could point toward a phenomenologically similar rheology, because strain rates are highest at the surface where the shear stress is the lowest and decrease with depth as stress presumably increases (Fig 2). There is no a priori expectation for solifluctuing soil to actually exhibit shear-thickening rheology akin to oobleck; in fact, soils and other dense geophysical suspensions have been shown to be able to exhibit a wide range of rheology, mostly shear thinning but occasionally shear thickening (*67*) or strain hardening (*19*). However, there is ample field evidence that solifluction terraces and lobes experience a slowdown in soil velocity right at the front and edges (e.g., Figure 2D). There are a variety of plausible mechanisms for this slowdown that do not rely on shear thickening rheology, most of which relate to soil moisture and/or cohesion (see Discussion in (*4*)). For example, field observations demonstrate enhanced drainage and a lower depth to groundwater table during fall freeze up at terrace fronts and lobe fronts/edges which may decrease both deformation due to frost heave and subsequent downslope motion in the spring (*39*). Conversely, once a front is formed, concentration of water during the spring may enhance vegetation growth and stabilize fronts (*17, 68*). Sediment compaction and enhanced cohesion due to capillary bridging may further impede motion at the front. Finally, differences in thermal state at the front could also modify frost heave efficiency (*68*) (Figure 10).

7.1 Linear Stability Analysis and Numerical Model

Based on these field observations and the need for a non-inertial source of instability, we use oobleck waves (*23, 66*) as inspiration for a possible analogous mechanism that relies not explicitly on soil rheology but topographically dependent properties of the soil (such as soil moisture, thermal state) that may alter effective viscosity near bumps.

For simplicity, our formulation assumes that the effective viscosity depends solely on the downslope gradient (dh/dx) of the free surface; though a dependence on depth is also likely (Section 6), here we isolate the bump-dependent aspect because including both makes the stability analysis prohibitively complex, and because we want to see whether a bump-dependent viscosity alone is enough to produce an instability. We envision that this bump-dependent formulation serves as a rough proxy for spatial variations in physical properties of the soil that control effective soil viscosity or velocity (described above).

We use this simple formulation:

$$\mu(x) = \mu_0 e^{-a\frac{\partial h}{\partial x}} \tag{25}$$

where a is a scaling factor, $\sin\theta$ is the slope of an inclined plane, and x is defined as increasing in the downhill direction. which results in higher viscosity when $\frac{\partial h}{\partial x}$ is negative (i.e., downhill facing bumps) and lower viscosity as $\frac{\partial h}{\partial x}$ increases (thus, uphill faces of bumps have an effectively lower viscosity; e.g., anecdotal field evidence shows surface ponding on lobe treads). This formulation is different from and far simpler than an accurate equation for a shear thickening suspension (e.g., (*69*)). We choose to use this highly simplified equation for μ to capture the essence of the proposed effect—bump dependent viscosity—without appealing to the specifics of rheology, because we simply do not have enough information to be confident in a specific rheology for

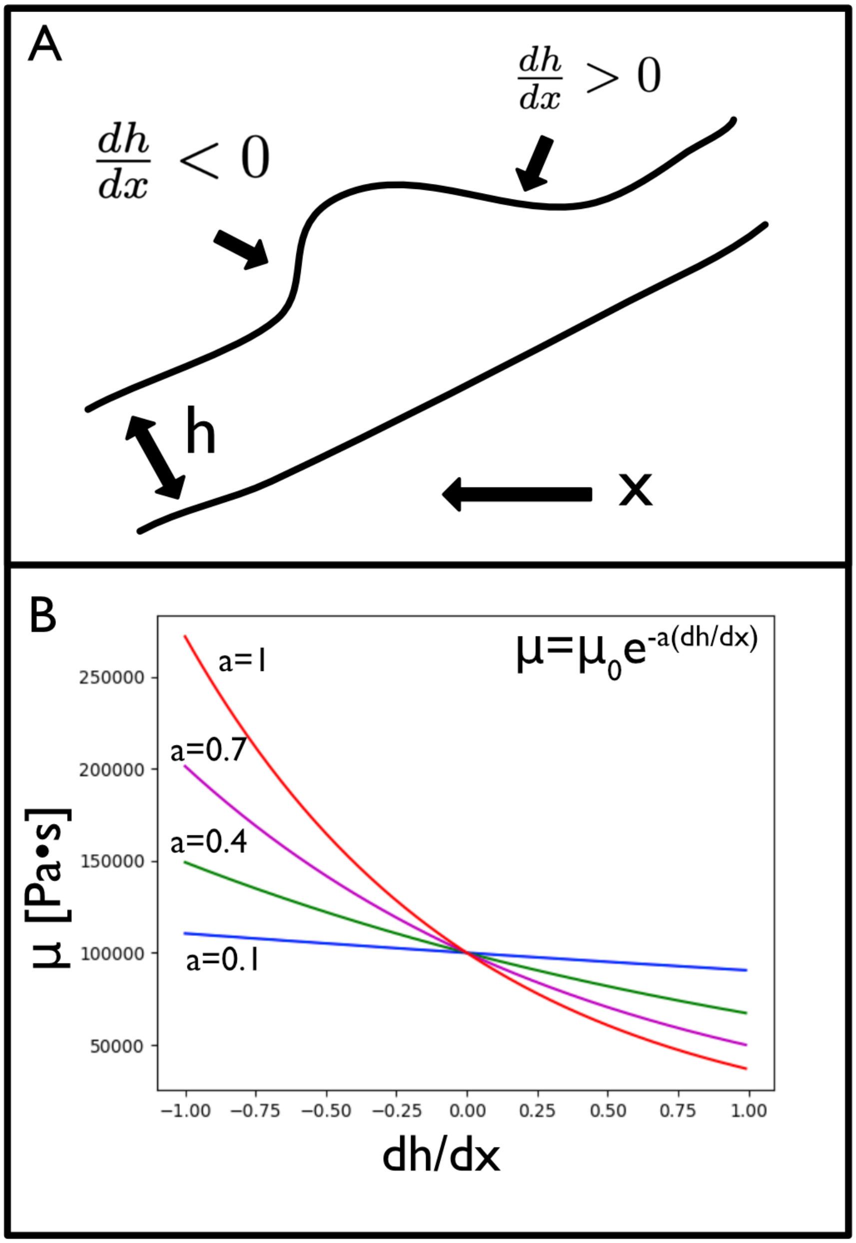

Figure 6: **Conceptual figure illustrating bump-dependent viscosity formulation.** (**A**) Conceptual sketch illustrating positive and negative dh/dx across a topographic bump. Note that x is defined to be positive toward the left in this figure so that it visually corresponds with the plot in part B. (**B**) corresponding viscosity μ for different values of scaling factor a, illusrating higher viscosity at negative dh/dx values (the downhill side of the bump) and lower viscosity at postivie dh/dx values (the uphill side of the bump). In this examples, $\mu_0 = 10^5 Pa \cdot s$.

solifluctuing soil (and it is most certainly not strictly oobleckian).

Plugging Eq. 25 into μ in Eq. 4, this results in a velocity profile as follows:

$$u(z) = \frac{\rho g(\sin\theta - \frac{dh}{dx})}{\mu_0 e^{-a\frac{dh}{dx}}}(hz - \frac{z^2}{2}) \tag{26}$$

According to continuity, the resulting governing equation is:

$$\frac{\partial H}{\partial t} = \frac{\rho g H^2}{3\mu_0} e^{a\frac{\partial H}{\partial x}} \left((1 - a\sin\theta)\, H\frac{\partial^2 H}{\partial x^2} + \frac{\partial H}{\partial x}\left(aH\frac{\partial^2 H}{\partial x^2} - 3\sin\theta \right) + 3(\frac{\partial H}{\partial x})^2 \right) \tag{27}$$

Even before conducting our stability analysis, we can see clues about the stability of Eqn. 27 by looking at the equation. A diffusion equation is stable if the diffusivity D¿0 and unstable in D¡0. Looking at the diffusive term $((1 - a\sin\theta)\, H\frac{\partial^2 H}{\partial x^2}$, we can see that the term is only stable when $1 - a\sin\theta$ is positive, or when $a\sin\theta < 1$. Further, the other term with $\frac{\partial^2 H}{\partial x^2}$ include a $\frac{\partial H}{\partial x}$ in front, meaning this diffusive term is only positive when $\frac{\partial H}{\partial x} > 0$. It is interesting to note that the $\frac{\partial^2 H}{\partial x^2}$ term is part of the famous KPZ equation used to describe surface growth and roughening processes (*70*).

Conducting a linear stability analysis (Supplementary Materials), we find:

$$\gamma = \frac{-\rho g h_0^3(1 - a\sin\theta)}{3\mu_0}k^2 + (\rho g h_0^2 3\sin\theta)ik \tag{28}$$

This result is (finally) more interesting than the previous analyses we showed! It has conditional stability; it is stable when $a\sin\theta < 1$, and unstable when $a\sin\theta > 1$. Unfortunately, however, the form of the resulting growth rate does not give a preferred wavelength- the growth rate when unstable increases monotonically. This may be due to finite amplitude effects, in which the nonlinear terms (which we ignored in our linear stability analysis) are needed to dampen small wavelengths.

7.2 Numerical Exploration

To explore this, we run a simple numerical model of the system in Matlab to explore stability and wavelength selection when all nonlinear terms are included (solving the continuity equation through time using Eq. 26 for the vertical velocity profile) (Supplementary Materials). The model domain is 100m long and consists of a hillslope with a set initial soil thickness h with a slope of 0.5, soil density = $1500 kg/m^3$, and initial viscosity $\mu_0 = 10^{10} Pa \cdot s$. We use a simple euler forward numerical scheme with a spatial step of 1m. The model is initialized with an uniform soil thickness (ranging from 1-3m) with random perturbations of soil thickness in each cell ranging from 0-.01m. The choice of timestep for stability depended on initial soil thickness and the exponential scaling parameter a as follows: for 1m soil, dt = 1/2000 years; for 2m soil with a=3, dt = 1/5000 years; for 2m soil with a=4,5,6, and 3m soil with a=3, dt=1/10,000 years; for 3m soil with a=4, dt = 20,000 years. See Supplementary Materials for model code. With the chosen parameters, flow velocities are roughly in line with solifluction velocities (tens of centimeters/year). While time evolution in the model seems very short (1 year), this cannot be directly compared to timescales in the field where soil is frozen stiff for half or more of the year, and most motion likely takes place within a short span of days or weeks during spring thaw.

We find that, as expected from our analysis, the system is stable for low values of $a \sin \theta$ and becomes unstable for values of $a \sin \theta > 1$. In contrast to our linear stability analysis, however, we observe a soil thickness dependence in the stability criterion such that increasing initial soil thickness requires lower values of $a \sin \theta$ to become unstable; for example, when initial soil thickness is 1m, the system becomes unstable only when $a \sin \theta > 2$. When initial soil thickness is 2 or 3m, we observe instability around $a \sin \theta > 1.5$ (Supplementary Videos). The dependence of stability on soil thickness and the slight deviation from our predicted critical value of 1 must stem from nonlinear terms that were removed in our linear stability analysis, of which there are many (Supplementary Materials).

Similar to the results seen for oobleck waves (*66*), our linear stability analysis predicted a monotonic increase in growth rate with wavenumber—that is, no preferred wavelength for instabilities. However, our numerical solution demonstrates more interesting behavior. Overall, we observe that the initial random perturbation in soil thickness rapidly self organizes into small, grid-scale waves that continuously coarsen through time (Figures 7, 8) (Supplementary Videos). This coarsening behavior indicates that the nonlinear terms in our governing equation are indeed important, and dominate over the expected behavior from linear stability analysis (e.g., (*71*)). Figure 8 illustrates the change in mean wavelength through time for model runs with three different initial thicknesses (1-3m) and 4 different values of scaling parameter a (3-6). All models presented in this figure used the same random seed for initial perturbations. Mean wavelength was simply calculated as the mean distance between peaks in soil thickness. Results show that mean wavelength increases through time for all cases, with a coarsening rate that increases with initial soil thickness. However,

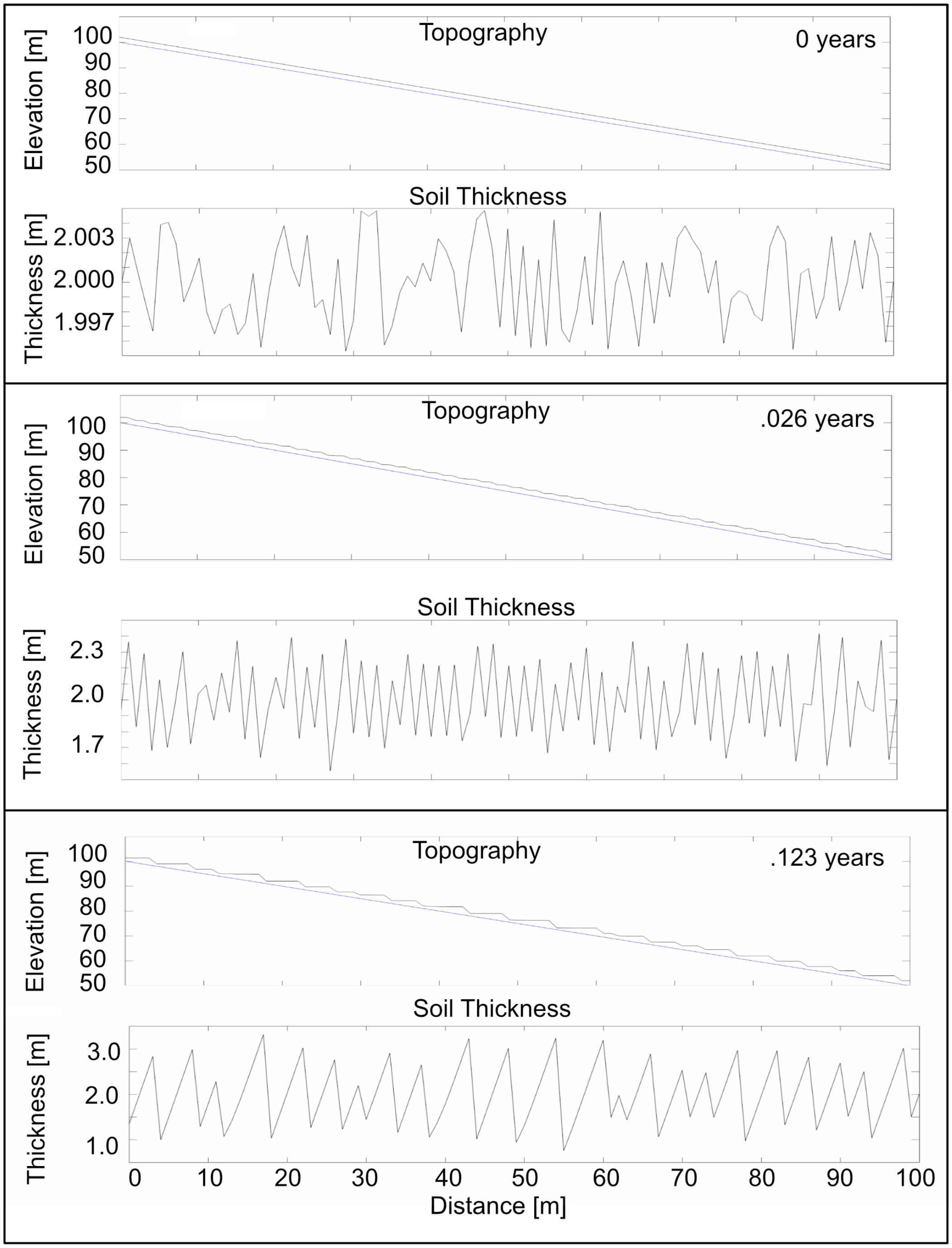

Figure 7: 1D numerical model of terrace formation using the viscosity formulation in Eqn. 26 shows organized waves developing through time.

mean wavelength decreases with increasing scaling parameter *a*—that is, the stronger the effect of bump-dependent viscosity, the smaller the resulting wavelength (similar to the fact that contact instability finger wavelength decreases as surface tension increases (*24*)). This makes sense from a conservation of mass standpoint—if a stronger viscosity effect limits the height at which bumps can continue to move, there can be a larger number of bumps (and therefore shorter wavelength). For a lower viscosity effect, bumps can continue to grow and coalesce into larger wavelengths.

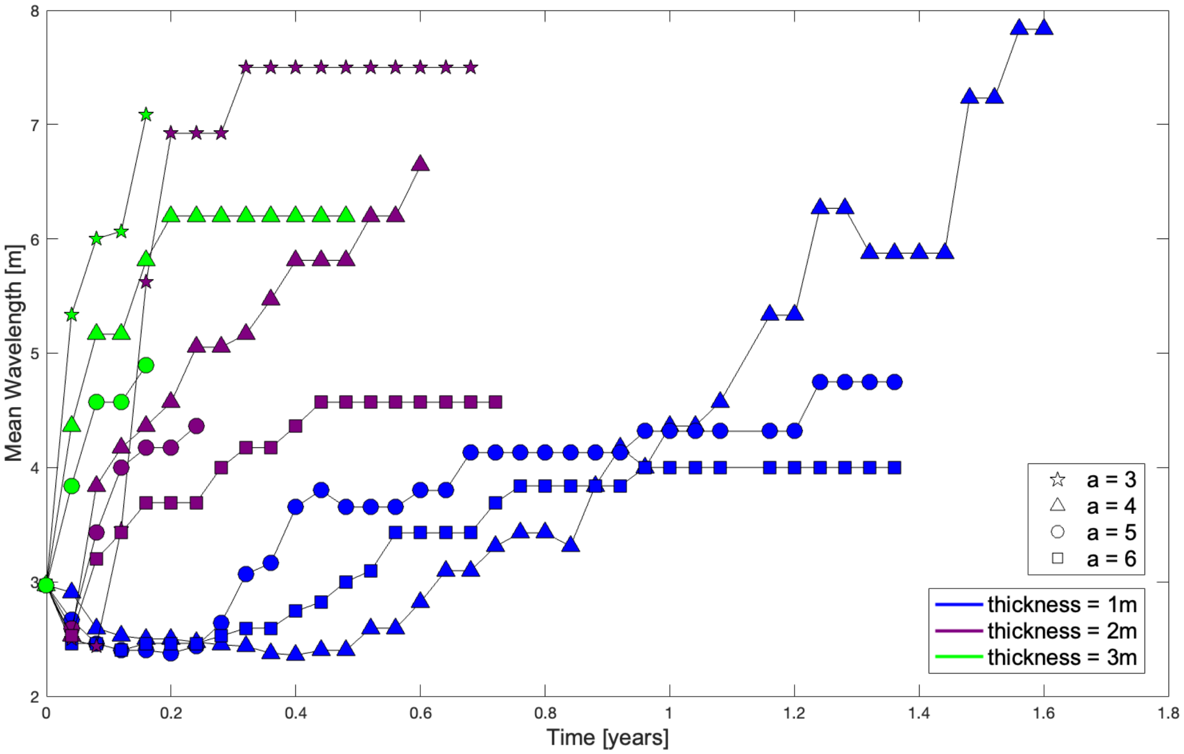

Figure 8: Evolution of mean wavelength through time for 1D model runs with different thickness (colors) and values of scaling parameter *a* (symbols).

Coarsening results in strikingly self-organized waves in all runs except for the lowest initial soil thickness of 1m with the lowest *a*, where the resulting waves are not evenly spaced (Supplementary Videos)). Figure 8 suggests that the “final” coarse wavelength might increase with increasing initial soil thickness (however, due to prohibitively long run times, we could not run the model to observe further coarsening). The long wavelengths seen for 1m thickness with a=4 are likely due to the fact that those waves were not uniformly spaced and well organized (Supplementary Video), perhaps because the low soil thickness and relatively low strength of the bump-dependent viscosity effect prevented clear organization. However, coarsening in our model does not continue indefinitely; at some point coarsened waves become stable and cease to evolve, likely due to 1) limited soil thickness available to transport and 2) a drastic increase in effective viscosity for tall waves such that the soil effectively becomes a solid. Regardless, it is clear that the increase in wave height and wavelength slows down, which can also be seen in videos of oobleck waves (*23*). In reality, it is likely that at a certain point the material ceases to behave like a fluid and obeys solid-like behavior, which may allow the front to eventually collapse and rebuild (Section 8; Figure 10). It is important to note that the wavelengths produced in our toy model are very likely dependent on the scale of the initial perturbation, which is set by the grid size. Similarly, in the field, there is likely a minimum size of perturbation required to initiate bump-dependent soil deformation rates.

Our numerical results show that the proposed simple bump-dependent viscosity formulation is capable of producing highly organized waves that strongly resemble solifluction terraces, importantly without appealing to inertia or multilayer flow. We avoid further formal analysis of this numerical model because we have no evidence that the precise governing equation (which as a reminder, we made up entirely) is valid for our system. Rather, this demonstration is to show that a formulation of this general type, with bump-dependent properties, may be enough to explain the formation of solifluction terraces. If we assume that our results are at all illustrative of what could happen in a solifluction system, one could imagine that the wavelengths observed in the field reflect a complex combination of soil thickness, frost-heave perturbation magnitude, strength of bump-dependent velocity effect, and time since initiation. Perhaps this explains why observations of solifluction wavelengths are so messy (Figure 4; (*4*)).

To explore potential 2D effects, we modified our 1D model of flow down an inclined plane to allow flow in the y (cross-slope) direction, using periodic boundary conditions in both the x and y direction with an initial soil thickness of 1.5m and a timestep of 1/20,000 years. When we use a bump-dependent viscosity in only the x (downhill) direction, with constant viscosity in the y direction, we observe the coalescence of nascent terraces into perfectly straight features that span the width of the domain (Figure 9A). We also explore the case of bump dependent viscosity in the y direction using the equation:

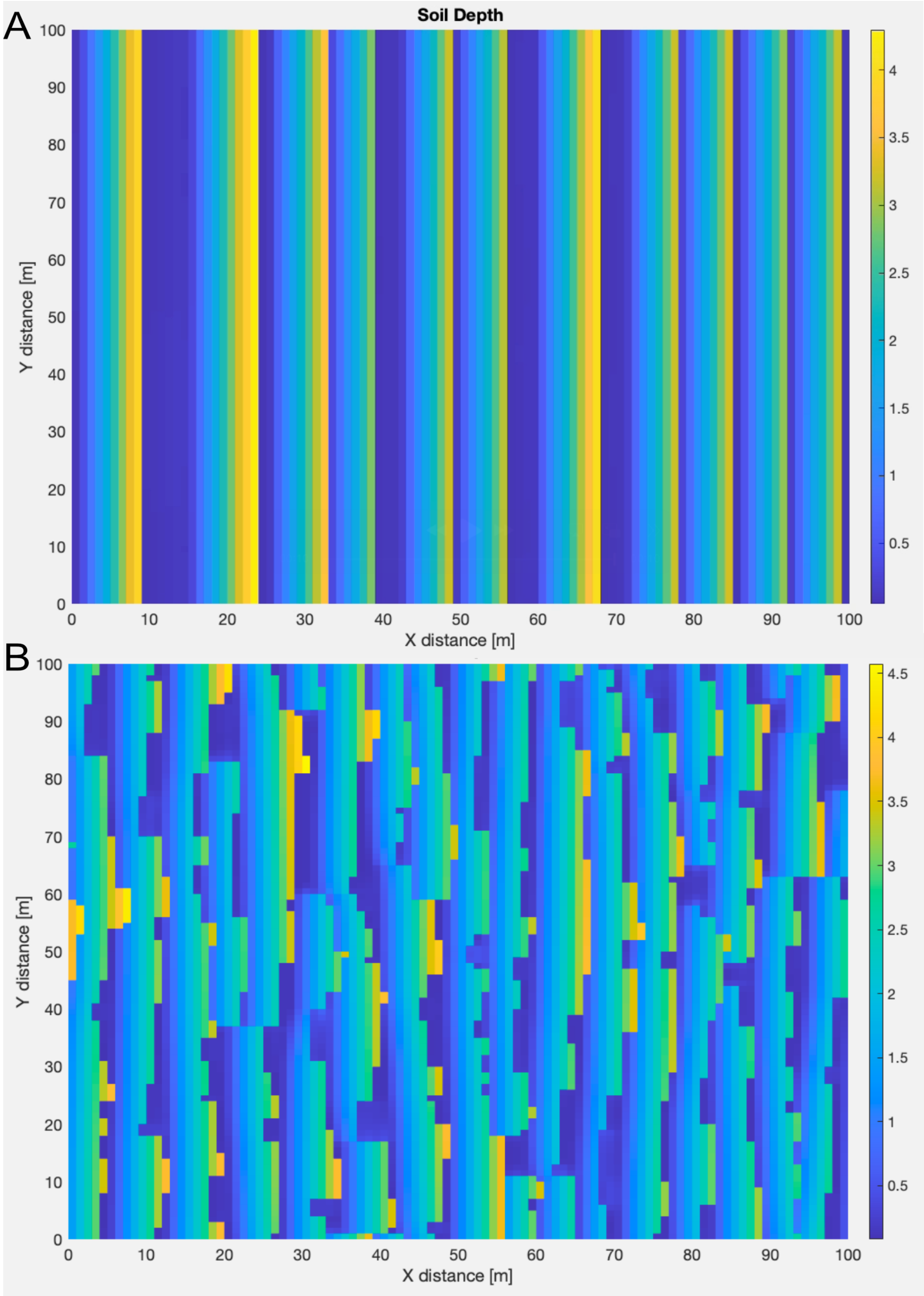

Figure 9: 2D model of terrace formation using a bump-dependent viscosity formulation. Flow is left to right. Initial soil depth is 1.5m. Colors indicate soil depth (meters). A) Bump dependent viscosity only in downhill x direction; constant viscosity in y direction. B) Bump dependent viscosity with the exponential viscosity parameter a = 5 in both the x (downhill) and y (cross slope) direction.

$$\mu(x) = \mu_0 e^{-a|\frac{\partial h}{\partial y}|} \tag{29}$$

This differs from the downhill viscosity formulation (Eqn. 25) in that bump dependent viscosity only depends on $|dh/dy|$, with no difference depending on the direction. With bump dependent viscosity in both the x and y direction, we observe the spontaneous formation of lobe-like features at terrace fronts (Figure 9B). However, cross-slope lobes are not highly organized in our model (i.e., we do not observe a characteristic wavelength). This may be due to the highly simplified 2D model in which soil can only move in 2 directions; perhaps a more advanced model allowing for D8 flow routing would produce more realistic lobes (Supplementary Videos). Of course, a more likely explanation is that our highly simplified model is not capturing the physics of real landscapes, and more complexity would be needed to fully reproduce the observed patterns. Regardless, the 2D model suggests that our bump dependent viscosity formulation has the potential to explain the development both downslope and cross-slope solifluction patterns—an enticing idea! Further, soil conditions and topography at different field sites may favor bump-dependent viscosity only in the downslope direction (resulting in smooth terraces, see Figure 1A and Figure 10) or in both downslope and cross-slope (Figure 1B).

7.3 What Sets Maximum Terrace and Lobe Height?

Our linear stability analysis numerical results show that terrace wavelength coarsening and increase in height may plausibly continue forever, albeit at a slower and slower rate through time as effective viscosity at the front becomes exceedingly high. However, we posit that at a certain height this behavior becomes unrealistic and the material begins to act much more like a solid than a fluid, with a maximum shear strength set by competition between cohesion, internal friction, and shear stress as viewed in classical soil mechanics. Indeed, recent remote observations indicate that soil instabilities may continue to grow until reaching a critical size, at which point failure mechanisms set in to arrest further growth. According to classic mohr-coulomb stability, the maximum height H of a vertical column of soil should scale inversely with gravity (*72*). Comparison of solifluction lobe height between Earth and Mars showed that lobes on Mars are approximately 2.6 times taller than those on Earth, the precise value expected if lobe height is set by the cohesive strength of the material under different gravitational conditions (*14*). This suggests that, in natural systems, a collapse triggered by reaching the soil's cohesive limit might be the mechanism that ultimately controls the amplitude of the instability. Indeed, many field studies provide evidence of collapse and subsequent advance of solifluction lobe fronts (*9, 53, 73–75*). (*53*) used radiocarbon dating to find that solifluction lobes build up behind a relatively stagnant front, then collapse, then rebuild again in a cycle of hundreds of years. Our work supports this conceptual model of solifluction lobe and terrace advance.

8 Conceptual model for solifluction pattern formation

Our work has shown many mechanisms (simple frost creep, buckling instabilities, roll waves) that *cannot* explain the onset of solifluction instabilities. While oobleck waves represent a potential analogous non-inertial system, we do not suggest directly comparing these systems because solifluction likely does not behave as a simple shear-thickening fluid; further, if rheology alone were the dominant factor in producing patterns, we may expect to see similar patterns in temperate landscapes (which to our knowledge have not been found). However, we suggest that there is a phenomenological similarity between the two in which a variety of conditions may cause slower soil velocities (and thus an effectively higher viscosity, if using a fluid framework) at the front of bumps, leading to the instability. As discussed above, many plausible natural mechanisms exist for this including spatial and temporal trends in soil moisture, vegetation, and granular compaction (*17, 34, 39, 40, 53, 68*).

After evaluating many different possible mechanisms, we propose the three following minimum necessary and sufficient ingredients for the initiation of solifluction-like patterns:

1) Initial roughness elements large enough to experience spatial heterogeneity in soil properties
2) Rheology or other mechanism (non-inertial) that causes slower soil velocity and therefore buildup at the fronts of these bumps
3) Fronts collapse once they become too tall, such that they move downhill

We propose that these three ingredients are enough to form not only downslope-oriented solifluction terraces, but likely subsequent soilfluction lobes that form at terrace fronts (Figure 9) (*4*). The simplicity and generalized nature of the three ingredients begs the question of why we only see solifluction patterns in cold places. None of the necessary and sufficient ingredients

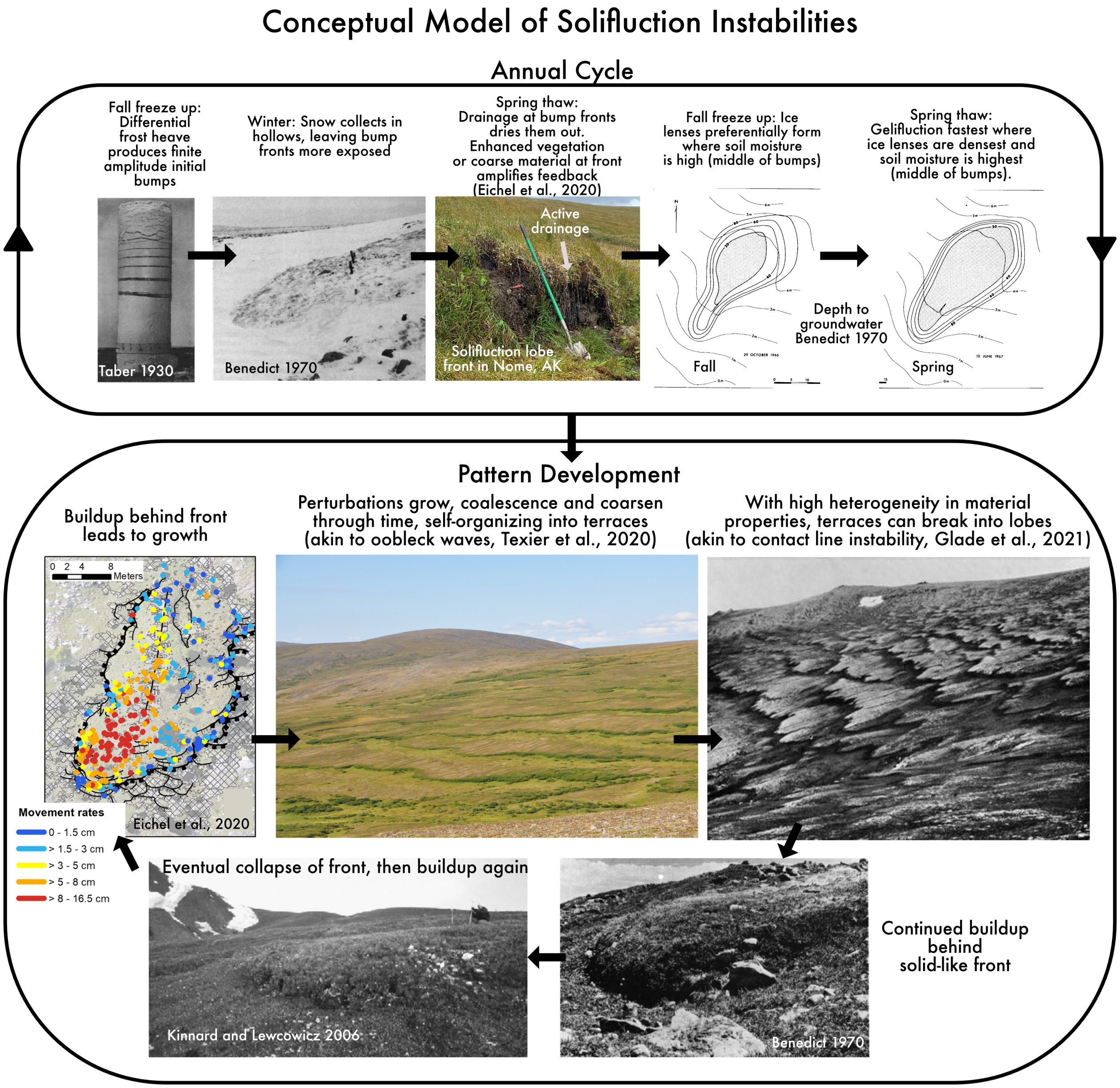

Figure 10: Conceptual model of solifluction instabilities. Top: Annual cycle of frost heave and soil moisture conditions leading to soil buildup behind bumps. Bottom: Buildup behind bumps leads to growth of patterns. Collapse of solid-like fronts allows motion downhill. Note: We use photographs of solifluction lobes in this figure because they are most abundant in the literature; however, illustrations represent roughness elements that ultimately lead to pattern formation.

above exclusively require ice or frost heave at first glance. However, we propose that it is only in cold (if not permafrost) landscapes that these key ingredients can be satisfied due to the unique annual processes that occur there on a regular basis. For the first ingredient, differential frost heave is a highly efficient creator of significant surface roughness, generating bumps up to a foot in height (*27*). While animals, tree throw, and other mechanisms generate roughness in temperate landscapes, frost heave is one of the only mechanisms that produces substantial roughness reliably every single year across the entire landscape. For the second ingredient, substantial differences in soil velocity are needed across a topographic bump. While there are many different mechanisms that could accomplish this (see above), by far the most likely would be due to differences in soil moisture across a bump and soil velocity that is closely connected to soil moisture. Frost creep and gelifluction are highly efficient, soil moisture-dependent processes that can only be found in cold places. While supersaturated soil on slopes can occur in temperate regions, this is generally due to rare large storms. In permafrost landscapes the presence of a relatively impermeable permafrost layer decreases the volume of soil that can accept water, and the soil reliably becomes saturated every year, with areas of high moisture content experiencing both higher frost heave in the winter and stronger gelifluction during spring thaw (*39*). It is also worth considering the idea that variations in subsurface characteristics, e.g. permafrost and groundwater depth, could lead to instability even in the presence of a flat surface topography. The third ingredient requires only that the soil has a maximum strength until it collapses, which should not require cold region dynamics.

We have summarized our detailed conceptual model in Figure 10. At the top of the figure, we illustrate the conditions that may lead to the first two ingredients: sufficient initial roughness and buildup behind bumps. After initial roughness is produced by frost heave in a landscape, we hypothesize that soil moisture conditions are the most important element for the second ingredient—buildup behind bumps—based on field observations and the fact that not all solifluction patterns are associated with clear vegetation or grain size segregation patterns (as is the case in stone-banked lobes). Snowfall during the winter tends to concentrate in hollows between bumps and areas of low slope (i.e., the uphill side of bumps), leaving the front of bumps more exposed. In the spring, this focuses thawed water flow into hollows, again leaving bumps drier. During fall freeze up, ice lenses preferentially form where soil moisture is high, which tends to be on the uphill side or middle of bumps but not the front. During spring thaw, gelifluction will be most efficient where frost heave was highest, leading to higher soil velocities behind the front of bumps. This cycle repeats every year, leading to growth of bumps and the possible development of solifluction patterns. When the bumps grow too tall, depending on their materials properties (cohesion, internal friction angle, grain size), slope and gravity, they collapse and build up again (Figure 10 bottom). We propose that the reason these patterns are only seen in cold places is that frost heave and gelifluction, in the presence of large quantities of snow, result in a hillslope system that is highly dependent on soil moisture and flow properties and which experiences strong spatial variations in these properties every year. In other landscapes, it is plausible that solifluction-like patterns could form, but these are more likely to be one-off features such as earth flows or small features after a particularly strong rainstorm. Additionally, the prevalence of diffusive-like disturbances in temperate landscapes (tree throw, gophers, ants, etc.) may destroy any features that begin to form.

A key difficulty in validating our conceptual model is the lack of field sites with clear proto-solifluction patterns. Though the timescale for pattern development is unknown, previous studies estimate that it may be hunderds of years (*34*). This makes real time observation of solifluction pattern initiation and development impossible with current technology. With high resolution satellite imagery it may be possible to observe initiation of patterns, but if so we would only have limited data currently of high enough resolution. The lack of proto-patterns is why we only show images of solifluction lobes for demonstration in Figure 10; however, note that these are illustrative and we believe the initial roughness would consist of smaller less-organizes bumps.

Still, targeted field measurements could test some of our findings. More studies like (*40*) could collect high resolution data on soil velocities and differences in material properties such as soil moisture, cohesion, and grain size within a solifluction terrace. Cores could be collected for geotechnical testing of rheological properties within solifluction terraces and lobes. Physical experiments, though challenging, could also speed up seasonal cycles and attempt to create solifluction patterns in the lab- something that's never been done before (*20*).

9 Conclusions

In this paper, we have used a combination of theory, numerical modeling, remote sensing, and literature review to explore many different plausible mechanisms for the initiation of solifluction terraces. We conclude that despite striking visual similarities, solifluction terraces are not examples of buckling instabilities or roll waves. They also cannot be explained by classic diffusive-like hillslope formulations. We find that the closest analogous pattern msy be oobleck waves, which form due to unique non-newtonian rheology that leads to an increase in effective viscosity on the downhill side of topographic bumps. We argue that solifluctíng soil may experience a phenomenologically similar instability in which spatial differences in soil moisture lead to differences in soil velocity, with buildup of soil behind the fronts of topographic bumps that leads to spatial organization of patterns. Based on prior work, we believe this mechanism can explain not only the initiation of solifluction terraces, but also of subsequent solifluction lobes that form at their fronts akin to a contact line instability (*4*). We hope our work demonstrates the vast potential of comparing geomorphic systems with those found in disparate fields such as fluid and solid mechanics and soft matter physics (*21*); however, we also hope the reader has gained an appreciation for the non-uniqueness of patterns and the many caveats that should be taken into consideration when comparing idealized physics problems with messy natural systems. It is both deeply humbling and inspiring that such a seemingly simple, slow-moving, soil-covered hill can be so engimatic and rich in behavior.

References and Notes

1. M. Kessler, B. Werner, Self-organization of sorted patterned ground. *Science* **299** (5605), 380–383 (2003).
2. A. H. Lachenbruch, *Mechanics of thermal contraction cracks and ice-wedge polygons in permafrost*, vol. 70 (Geological Society of America) (1962).
3. N. Matsuoka, Solifluction rates, processes and landforms: a global review. *Earth-Science Reviews* **55** (1-2), 107–134 (2001).
4. R. C. Glade, M. M. Fratkin, M. Pouragha, A. Seiphoori, J. C. Rowland, Arctic soil patterns analogous to fluid instabilities. *Proceedings of the National Academy of Sciences* **118** (21), e2101255118 (2021).
5. J. G. Andersson, Solifluction, a component of subaerial denudation. *The Journal of Geology* **14** (2), 91–112 (1906).
6. A. Rempel, Formation of ice lenses and frost heave. *Journal of Geophysical Research: Earth Surface* **112** (F2) (2007).
7. S. S. Peppin, R. W. Style, The physics of frost heave and ice-lens growth. *Vadose Zone Journal* **12** (1), 1–12 (2013).
8. R. S. Anderson, S. P. Anderson, *Geomorphology: the mechanics and chemistry of landscapes* (Cambridge University Press) (2010).
9. J. B. Benedict, Frost creep and gelifluction features: a review. *Quaternary Research* **6** (1), 55–76 (1976).
10. C. Harris, M. C. Davies, Gelifluction: observations from large-scale laboratory simulations. *Arctic, Antarctic, and Alpine Research* **32** (2), 202–207 (2000).
11. H. M. French, *The periglacial environment* (John Wiley & Sons) (2017).

12. R. Gastineau, *et al.*, Small-scale lobate hillslope features on Mars: A comparative 3D morphological study with terrestrial solifluction lobes and zebra stripe lobes. *Icarus* **342**, 113606 (2020).

13. A. Johnsson, *et al.*, Periglacial mass-wasting landforms on Mars suggestive of transient liquid water in the recent past: Insights from solifluction lobes on Svalbard. *Icarus* **218** (1), 489–505 (2012).

14. J. Sleiman, S. Conway, A. Johnsson, J. Wray, R. Glade, Viewing Lobate Patterns on Mars and Earth as Climate Modulated Fluid-like Instabilities (2024).

15. J. Rowland, *et al.*, Arctic landscapes in transition: responses to thawing permafrost. *Eos, Transactions American Geophysical Union* **91** (26), 229–230 (2010).

16. M. Harkema, W. Nijland, S. de Jong, T. Kattenborn, J. Eichel, Monitoring solifluction movement in space and time: A semi-automated high-resolution approach. *Geomorphology* **433**, 108727 (2023).

17. D. Draebing, J. Eichel, Spatial controls of turf-banked solifluction lobes and their role for paraglacial adjustment in glacier forelands. *Permafrost and Periglacial Processes* **28** (2), 446–459 (2017).

18. C. Harris, Physical modelling of periglacial solifluction: Review and future strategy. *Permafrost and Periglacial Processes* **7** (4), 349–360 (1996).

19. C. Harris, M. C. Davies, B. R. Rea, Gelifluction: viscous flow or plastic creep? *Earth Surface Processes and Landforms: The Journal of the British Geomorphological Research Group* **28** (12), 1289–1301 (2003).

20. C. Harris, *et al.*, Solifluction processes on permafrost and non-permafrost slopes: results of a large-scale laboratory simulation. *Permafrost and Periglacial Processes* **19** (4), 359–378 (2008).

21. D. J. Jerolmack, K. E. Daniels, Viewing Earth's surface as a soft-matter landscape. *Nature Reviews Physics* **1** (12), 716–730 (2019).

22. R. W. Griffiths, The dynamics of lava flows. *Annual review of fluid mechanics* **32** (1), 477–518 (2000).

23. B. Darbois Texier, H. Lhuissier, Y. Forterre, B. Metzger, Surface-wave instability without inertia in shear-thickening suspensions. *Communications Physics* **3** (1), 232 (2020).

24. H. E. Huppert, Flow and instability of a viscous current down a slope. *Nature* **300** (5891), 427–429 (1982).

25. N. S. Deshpande, D. J. Furbish, P. E. Arratia, D. J. Jerolmack, The perpetual fragility of creeping hillslopes. *Nature Communications* **12** (1), 3909 (2021).

26. L. Pawlik, P. Šamonil, Soil creep: the driving factors, evidence and significance for biogeomorphic and pedogenic domains and systems–a critical literature review. *Earth-Science Reviews* **178**, 257–278 (2018).

27. S. Taber, The mechanics of frost heaving. *The Journal of Geology* **38** (4), 303–317 (1930).

28. N. Matsuoka, K. Hirakawa, Solifluction resulting from one-sided and two-sided freezing: field data from Svalbard. *Polar geoscience* **13**, 187–201 (2000).

29. C. K. Ballantyne, A 35-year record of solifluction in a maritime periglacial environment. *Permafrost and Periglacial Processes* **24** (1), 56–66 (2013).

30. D. J. Smith, Rates and controls of soil movement on a solifluction slope in the Mount Rae area, Canadian Rocky Mountains. *Zeitschrift für Geomorphologie NF* **71**, 25–44 (1988).

31. L. W. Price, Subsurface movement on solifluction slopes in the Ruby Range, Yukon Territory, Canada—a 20-year study. *Arctic and Alpine Research* **23** (2), 200–205 (1991).

32. N. Matsuoka, A. Ikeda, T. Date, Morphometric analysis of solifluction lobes and rock glaciers in the Swiss Alps. *Permafrost and Periglacial Processes* **16** (1), 99–113 (2005).

33. N. Matsuoka, Solifluction and mudflow on a limestone periglacial slope in the Swiss Alps: 14 years of monitoring. *Permafrost and periglacial processes* **21** (3), 219–240 (2010).

34. C. Kinnard, A. G. Lewkowicz, Movement, moisture and thermal conditions at a turf-banked solifluction lobe, Kluane Range, Yukon Territory, Canada. *Permafrost and Periglacial Processes* **16** (3), 261–275 (2005).

35. C. Harris, M. C. Davies, J.-P. Coutard, Rates and processes of periglacial solifluction: an experimental approach. *Earth Surface Processes and Landforms: The Journal of the British Geomorphological Group* **22** (9), 849–868 (1997).

36. N. Matsuoka, K. Moriwaki, Frost heave and creep in the Sør Rondane Mountains, Antarctica. *Arctic and Alpine Research* **24** (4), 271–280 (1992).

37. S. Fiolleau, *et al.*, Insights on seasonal solifluction processes in warm permafrost Arctic landscape using a dense monitoring approach across adjacent hillslopes. *Environmental Research Letters* **19** (4), 044021 (2024).

38. M. Houssais, C. P. Ortiz, D. J. Durian, D. J. Jerolmack, Rheology of sediment transported by a laminar flow. *Physical Review E* **94** (6), 062609 (2016).

39. J. B. Benedict, Downslope soil movement in a Colorado alpine region: rates, processes, and climatic significance. *Arctic and Alpine Research* **2** (3), 165–226 (1970).

40. J. Eichel, *et al.*, Unmanned aerial vehicle-based mapping of turf-banked solifluction lobe movement and its relation to material, geomorphometric, thermal and vegetation properties. *Permafrost and Periglacial Processes* **31** (1), 97–109 (2020).

41. N. B. Coffey, *et al.*, Enigmatic surface rolls of the Ellesmere Ice Shelf. *Journal of Glaciology* **68** (271), 867–878 (2022).

42. M. A. Biot, Theory of folding of stratified viscoelastic media and its implications in tectonics and orogenesis. *Geological Society of America Bulletin* **72** (11), 1595–1620 (1961).

43. N. M. Ribe, E. Stutzmann, Y. Ren, R. Van Der Hilst, Buckling instabilities of subducted lithosphere beneath the transition zone. *Earth and Planetary Science Letters* **254** (1-2), 173–179 (2007).

44. N. J. Balmforth, R. Craster, A. C. Slim, On the buckling of elastic plates. *The Quarterly Journal of Mechanics & Applied Mathematics* **61** (2), 267–289 (2008).

45. N. M. Ribe, Coiling of viscous jets. *Proceedings of the Royal Society of London. Series A: Mathematical, Physical and Engineering Sciences* **460** (2051), 3223–3239 (2004).

46. D. S. Loewenherz, C. J. Lawrence, R. L. Weaver, On the development of transverse ridges on rock glaciers. *Journal of Glaciology* **35** (121), 383–391 (1989).

47. A. C. Slim, J. Teichman, L. Mahadevan, Buckling of a thin-layer Couette flow. *Journal of fluid mechanics* **694**, 5–28 (2012).

48. Q. Wang, X. Zhao, A three-dimensional phase diagram of growth-induced surface instabilities. *Scientific reports* **5** (1), 8887 (2015).

49. N. M. Ribe, Periodic folding of viscous sheets. *Physical Review E* **68** (3), 036305 (2003).

50. M. Skorobogatiy, L. Mahadevan, Folding of viscous sheets and filaments. *Europhysics Letters* **52** (5), 532 (2000).

51. K. Blake, A. Bejan, Experiments on the buckling of thin fluid layers undergoing end-compression (1984).

52. S. H. Treagus, Buckling stability of a viscous single-layer system, oblique to the principal compression. *Tectonophysics* **19** (3), 271–289 (1973).

53. C. Kinnard, A. G. Lewkowicz, Frontal advance of turf-banked solifluction lobes, Kluane Range, Yukon Territory, Canada. *Geomorphology* **73** (3-4), 261–276 (2006).

54. J. Del Vecchio, *et al.*, Patterns and rates of soil movement and shallow failures across several small watersheds on the Seward Peninsula, Alaska. *Earth Surface Dynamics Discussions* **2022**, 1–28 (2022).

55. J. Fink, Surface folding and viscosity of rhyolite flows. *Geology* **8** (5), 250–254 (1980).

56. P. L. Kapitza, Wave flow of thin viscous liquid films. III. Experimental study of wave regime of a flow. *J. Exp. Theor. Phys.* **19** (2), 105–120 (1949).

57. H.-C. Chang, *et al.*, Wave evolution on a falling film. *Annual review of fluid mechanics* **26** (1), 103–136 (1994).

58. N. Balmforth, J. Liu, Roll waves in mud. *Journal of Fluid Mechanics* **519**, 33–54 (2004).

59. M. K. Smith, The mechanism for the long-wave instability in thin liquid films. *Journal of Fluid Mechanics* **217**, 469–485 (1990).

60. F. Depoilly, S. Millet, H. Ben Hadid, S. Dagois-Bohy, F. Rousset, Unifying the roll waves. *PloS one* **19** (11), e0310805 (2024).

61. É. Guazzelli, O. Pouliquen, Rheology of dense granular suspensions. *Journal of Fluid Mechanics* **852**, P1 (2018).

62. D. J. Furbish, *et al.*, Rarefied particle motions on hillslopes–Part 1: Theory. *Earth Surface Dynamics* **9** (3), 539–576 (2021).

63. S. Chandrasekhar, *Hydrodynamic and hydromagnetic stability* (Courier Corporation) (2013).

64. J. A. Whitehead, Fluid models of geological hotspots. *Annual Review of Fluid Mechanics* **20** (1), 61–87 (1988).

65. P. Jop, Y. Forterre, O. Pouliquen, A constitutive law for dense granular flows. *Nature* **441** (7094), 727–730 (2006).

66. B. D. Texier, H. Lhuissier, B. Metzger, Y. Forterre, Shear-thickening suspensions down inclines: from Kapitza to Oobleck waves. *Journal of Fluid Mechanics* **959**, A27 (2023).

67. S. Pradeep, P. E. Arratia, D. J. Jerolmack, Origins of complexity in the rheology of Soft Earth suspensions. *Nature communications* **15** (1), 7432 (2024).

68. J. Eichel, *et al.*, Solifluction meets vegetation: the role of biogeomorphic feedbacks for turf-banked solifluction lobe development. *Earth Surface Processes and Landforms* **42** (11), 1623–1635 (2017).

69. M. Wyart, M. E. Cates, Discontinuous shear thickening without inertia in dense non-Brownian suspensions. *Physical review letters* **112** (9), 098302 (2014).

70. M. Hairer, Solving the KPZ equation. *Annals of mathematics* pp. 559–664 (2013).

71. P. Politi, C. Misbah, Nonlinear dynamics in one dimension: A criterion for coarsening and its temporal law. *Physical Review E—Statistical, Nonlinear, and Soft Matter Physics* **73** (3), 036133 (2006).

72. A. Abramian, L. Staron, P.-Y. Lagrée, The slumping of a cohesive granular column: Continuum and discrete modeling. *Journal of Rheology* **64** (5), 1227–1235 (2020).

73. P. Williams, Some investigations into solifluction features in Norway. *The Geographical Journal* **123** (1), 42–55 (1957).

74. H. Ridefelt, J. Boelhouwers, T. Eiken, Measurement of solifluction rates using multi-temporal aerial photography. *Earth Surface Processes and Landforms* **34** (5), 725–737 (2009).

75. H. Ridefelt, J. Boelhouwers, Observations on regional variation in solifluction landform morphology and environment in the Abisko region, northern Sweden. *Permafrost and Periglacial Processes* **17** (3), 253–266 (2006).

76. C. Harris, The role of climatic and soil properties in periglacial solifluction: Evidence from laboratory simulation experiments. *Solifluction and Climatic Variations in the Holocene, Special Issue: ESF Project European Paleoclimate and Man* (1993).

77. M. Fratkin, *et al.*, *Arctic soil patterns analogous to fluid instabilities: Supporting data*, Tech. rep., Environmental System Science Data Infrastructure for a Virtual Ecosystem . . . (2021).

Acknowledgments

Funding: Packard Science and Technology Fellowship (R.C.G., J.S.)

Author contributions: R.C.G.: Conceptualization, Funding, Data Analysis, Coding, Thoery, Visualization, Writing, Editing. J.S.: Data Collection, Editing. A.Q.: Theory, Editing. D.C.: Theory, Editing. S.W.: Theory, Editing.

Competing interests: There are no competing interests to declare.

Data and materials availability: All data and code are provided in the Supplementary Materials.

Supplementary materials

Materials and Methods

Movies S1-S3

Data S1-S6

Supplementary Materials for

Exploring Potential Mechanisms for the Initiation of Solifluction Patterns

Rachel C. Glade*, *Corresponding author. Email: rachel.glade@rochester.edu

This PDF file includes:

Materials and Methods

Captions for Movies S1 to S3

Captions for Data S1 to S6

Other Supplementary Materials for this manuscript:

Movies S1 to S3

Data S1 to S6

Materials and Methods

Depth-dependent viscosity formulation

Let u be the x-directed velocity, μ be the dynamic viscosity, μ_0 be a characteristic viscosity, $s = \sin\theta$ be the underlying slope, τ be the shear stress, z be the depth (where z=0 at the base and z=h at the surface), a be the viscosity scaling with depth, and h be the flow thickness. Note that wherever we write h, we imply $h(x)$.

$$\tau = \mu \frac{du}{dz} \tag{S1}$$

$$\tau = \rho g(h-z)\sin\theta - \rho g(h-z)\frac{dh}{dx} \tag{S2}$$

$$\mu = \mu_0 e^{a(h-z)} \tag{S3}$$

$$\frac{du}{dz} = \frac{\rho g(h-z)\sin\theta - \rho g(h-z)\frac{dh}{dx}}{\mu_0 e^{a(h-z)}} \tag{S4}$$

Boundary condition: u=0 @ z=0:

$$u(z) = \frac{\rho g(\sin\theta - \frac{dh}{dx})}{\mu_0}\left[\frac{e^{a(z-h)}(a(h-z)+1) - e^{-ah}(ah+1)}{a^2}\right] \tag{S5}$$

Mean value theorem:

$$\bar{u} = \frac{1}{h}\int_0^h u dz \tag{S6}$$

Plugging S5 into S6 we find:

$$\bar{u} = \frac{\rho g(\sin\theta - \frac{dh}{dx})}{h\mu_0}\left[\frac{2 - e^{-ah}(ah+2)}{a^3} - \frac{he^{-ah}(ah+1)}{a^2}\right] \tag{S7}$$

$$q = h\bar{u} = \frac{\rho g(\sin\theta - \frac{dh}{dx})}{\mu_0}\left[\frac{2 - e^{-ah}(ah+2)}{a^3} - \frac{he^{-ah}(ah+1)}{a^2}\right] \tag{S8}$$

Continuity:

$$\frac{\partial h}{\partial t} = -\frac{\partial q}{\partial x} \tag{S9}$$

$$\begin{aligned}\frac{dh}{dt} = \frac{2pg}{\mu_0 a^3}\frac{d^2h}{dx^2} - \frac{2\rho g e^{-ah}}{\mu_0 a^3}\frac{d^2h}{dx^2} - \frac{\rho g h e^{-ah}}{\mu_0 a^2}\frac{d^2h}{dx^2} \\ +\frac{\rho g e^{-ah}}{\mu_0 a^2}(\frac{dh}{dx})^2 + \frac{\rho g h e^{-ah}}{\mu_0 a}(\frac{dh}{dx})^2 \\ -\frac{\rho g h e^{-ah}}{\mu_0 a^2}\frac{d^2h}{dx^2} - \frac{\rho g e^{-ah}}{\mu_0 a^2}(\frac{dh}{dx})^2 - \frac{\rho g h^2 e^{-ah}}{\mu_0 a}\frac{d^2h}{dx^2} \\ -\frac{\rho g s h^2 e^{-ah}}{\mu_0}\frac{dh}{dx} + \frac{\rho g h^2 e^{-ah}}{\mu_0}(\frac{dh}{dx})^2 - \frac{\rho g h e^{-ah}}{\mu_0 a}(\frac{dh}{dx})^2\end{aligned} \tag{S10}$$

Then we retaining only first order terms because higher order terms (e.g., multiples of derivatives are neglible). Then Let:

$$h(x,t) = h_0 + h_1(x,t) \tag{S11}$$

Plugging this into S10, linearizing $e^{a(h_0+h_1)}$ to $e^{ah_0}(1 + ah_1)$ and keeping only terms linear in h_1 we find:

$$\begin{aligned}\frac{\partial h_1}{\partial t} = \frac{2\rho g}{\mu_0 a^3}\frac{d^2h_1}{dx^2} - \frac{2\rho g e^{-ah_0}}{\mu_0 a^3}\frac{d^2h_1}{dx^2} - \frac{\rho g h_0 e^{-ah_0}}{\mu_0 a^2}\frac{d^2h_1}{dx^2} - \frac{\rho g h_0 e^{-ah_0}}{\mu_0 a^2}\frac{d^2h_1}{dx^2} \\ -\frac{\rho g h_0^2 e^{-ah_0}}{\mu_0 a}\frac{d^2h_1}{dx^2} - \frac{\rho g s h_0^2 e^{-ah_0}}{\mu_0}\frac{dh_1}{dx}\end{aligned} \tag{S12}$$

We assume a solution of the form:

$$h_1 = Ae^{\gamma t + ikx} \tag{S13}$$

For reference, the relevant derivatives are:

$$\frac{\partial H_1}{\partial x} = A_0 ike^{\gamma t + ikx} \tag{S14}$$

$$\frac{\partial^2 H_1}{\partial x^2} = -A_0 k^2 e^{\gamma t + ikx} \tag{S15}$$

$$\frac{\partial H_1}{\partial t} = A_0 \gamma e^{\gamma t + ikx} \tag{S16}$$

Plugging these into S12 we find an expression for the growth rate γ:

$$\gamma = \left[\frac{2\rho g(e^{-ah_0}-1)}{\mu_0 a^3} + \frac{2\rho g h_0 e^{-ah_0}}{\mu_0 a^2} + \frac{\rho g h_0^2 e^{-ah_0}}{\mu_0 a}\right] k^2 - \left(\frac{\rho g s h_0^2 e^{-ah_0}}{\mu_0}\right) ik \tag{S17}$$

To evaluate the stability of the real part of the growth rate, let's let $b = ah_0$. All parameters $(\rho, g, mu_0, a, h_0) > 0$. Then we have:

$$f(b) = \frac{\rho g}{\mu_0 a^3}\left(2e^{-b} - 2 + 2xe^{-b} + x^2 e^{-b}\right) \tag{S18}$$

We wish to find the inflection points of this equation to determine when it is positive and when it is negative. Taking the derivative we get:

$$\frac{df}{db} = \frac{\rho g}{\mu_0 a^3}\left(2e^{-b} + 2be^{-b}(b-1) - be^{-b}(b-2)\right) \tag{S19}$$

Setting this equal to 0 and simplifying, we find:

$$-e^{-b}b^2 = 0 \tag{S20}$$

The only solution is when b = 0. This means that there are no inflection points, and the equation monotonically changes. We can see from S18 that as b increases, f(b) will only decrease due to the exponential terms. Therefore, the real part of the growth rate is negative for all values of ah_0, and therefore the system is unconditionally stable.

Bump-dependent viscosity formulation

$$\tau = \mu \frac{du}{dz} \tag{S21}$$

$$\tau = \rho g(h-z)\sin\theta - \rho g(h-z)\frac{dh}{dx} \tag{S22}$$

$$\mu = \mu_0 e^{-a\frac{dh}{dx}} \tag{S23}$$

$$\frac{du}{dz} = \frac{\rho g(h-z)\sin\theta - \rho g(h-z)\frac{dh}{dx}}{\mu_0 e^{-a\frac{dh}{dx}}} \tag{S24}$$

$$u(z) = \frac{\rho g(\sin\theta - \frac{dh}{dx})}{\mu_0 e^{-a\frac{dh}{dx}}}(hz - \frac{z^2}{2}) \tag{S25}$$

$$\bar{u} = \frac{\rho g h^2(\sin\theta - \frac{dh}{dx})}{3\mu_0 e^{-a\frac{dh}{dx}}} \tag{S26}$$

$$q = h\bar{u} = \frac{\rho g h^3(\sin\theta - \frac{dh}{dx})}{3\mu_0 e^{-a\frac{dh}{dx}}} \tag{S27}$$

$$\frac{\partial h}{\partial t} = -\frac{\partial q}{\partial x} \tag{S28}$$

$$\frac{\partial h}{\partial t} = h^2 e^{a\frac{\partial h}{\partial x}}((1 - a\sin\theta)h\frac{\partial^2 h}{\partial x^2} + \frac{\partial h}{\partial x}(ah\frac{\partial^2 h}{\partial x^2} - 3\sin\theta) + 3\frac{\partial h}{\partial x})^2) \tag{S29}$$

Get rid of multiples of derivatives. Then Let:

$$h(x,t) = h_0 + h_1(x,t) \tag{S30}$$

Keep only terms linear in h_1:

$$\frac{\partial h_1}{\partial t} = h_0^3(1 - a\sin\theta)\frac{\partial^2 h}{\partial x^2} - 3h_0^2\sin\theta\frac{\partial h}{\partial x} \tag{S31}$$

assume solution of the form:

$$h_1 = Ae^{\gamma t + ikx} \tag{S32}$$

$$\gamma = -\frac{\rho g h_0^3}{3\mu_0}(1 - a\sin\theta)k^2 + i\frac{\rho g h_0^2}{\mu}\sin\theta k \tag{S33}$$

Solifluction velocity data

Figure 2 was produced using data from numerous field and experiment studies (*28–35, 37, 76*). Data (Data S1) were estimated from plots in these studies using WebPlotDigitizer. Exponential profiles were normalized by calculating an e-folding depth to collapse data. Non-exponential profiles were normalized by the maximum velocity and depth of movement for each profile (Data S2).

Remote Sensing Analysis

Remote sensing data were collected in a previous study (*4*) from freely available Norwegian LiDAR data (https://hoydedata.no/LaserInnsyn2/) as follows. Hand-drawn 1D downslope elevation profiles were collected from submeter LiDAR-derived digital elevation models from 30 solifluction patterned hillslopes across Norway. The front of solifluction terraces was manually marked on these profiles. Solifluction terrace height was calculated by detrending elevation profiles according to the mean topographic slope of each profile and measuring the vertical height difference between the terrace front and the next downslope grid cell. Wavelength was measured as the mean distance between terrace fronts along each downslope profile (Data S1, Data s2). Original DEMs can be downloaded from (*77*).

Caption for Movie S1. Movie of 1D numerical model of solifluction terraces. Initial soil thickness = 2m; a = 5.

Caption for Movie S2. Movie of 2D numerical model of solifluction terraces. Bump-dependent viscosity only in x (downslope) direction. Initial soil thickness = 1.5m; a = 5.

Caption for Movie S3. Movie of 2D numerical model of solifluction terraces. Bump-dependent viscosity in both x (downslope) and y (cross-slope) direction. Initial soil thickness = 1.5m; a = 5.

Caption for Data S1. CSV files containing vertical solifluction velocity profiles

Caption for Data S2. Python script to plot solifluction velocity profiles in Figure 2.

Caption for Data S3. CSV file containing remote sensing terrace wavelength, height, and slope data

Caption for Data S4. Python script to plot terrace scaling data

Caption for Data S5. .m file with 1D Matlab numerical model of terrace formation

Caption for Data S6. .m file with 2D Matlab numerical model of terrace formation